Published by
NIGERIAN SOCIETY OF PHYSICAL SCIENCES
Available online @ https://asr.nsps.org.ng/index.php/asr

African Scientific Reports 5 (2026) 488

African Scientific Reports

Numerical optimization of photovoltaic performance of cesium titanium bromide perovskite solar cells using dual copper oxide hole transport layers

P. R. Jubu[a,b], O. D. Abi[c], Z. S. Mbalaha[b], I. K. Nwokolo[a], A. O. Aransiola[a,d], C. Amakom[a,e], K. Udofia[a,f], A. A. Goje[a,g], I. I. Ayogu[a], D. S. Igba[b], M. M. Gururani[h], E. E. Oguzie[a,i,*]

[a]*Africa Centre of Excellence in Future Energies and Electrochemical Systems (ACE-FUELS), Federal University of Technology Owerri (FUTO), P.M.B. 1526 Owerri, Imo State, Nigeria*
[b]*Department of Industrial Physics, Joseph Sarwuan Tarka University Makurdi (Federal University of Agriculture Makurdi) P.M.B. 2373, Makurdi, Benue State, Nigeria*
[c]*Department of Physics, Joseph Sarwuan Tarka University P.M.B. 2373, Makurdi, Benue State, Nigeria*
[d]*Department of Electronic and Electrical Engineering, Obafemi Awolowo University, Ile-Ife, Nigeria*
[e]*Department of Physics, Federal University of Technology Owerri (FUTO), P.M.B. 1526 Owerri, Imo State, Nigeria*
[f]*Department of Physics, Akwa Ibom State University, Akwa Ibom State, Nigeria*
[g]*Department of Applied Physics, Federal Polytechnic Damaturu, Nigeria*
[h]*Department of Physics, M.B. Government P.G. College, Haldwani (Uttarakhand), India*
[i]*Department of Chemistry, Federal University of Technology Owerri (FUTO), P.M.B. 1526 Owerri, Imo State, Nigeria*

Abstract

This work provides a comprehensive numerical evaluation by using SCAPS-1D software for designing efficient lead-free Cs_2TiBr_6-based perovskite solar cells (PSCs) based on all-inorganic carrier transport layers. The copper oxide hole transport layer (HTL) is introduced in the Cs_2TiBr_6-based PSC for the first time, recording a power conversion efficiency (PCE) that is superior to the values reported in the literature. The prototype FTO/CeO_x/Cs_2TiBr_6/Cu_2O/CuO/Au cell achieved a power conversion efficiency (PCE) of 8.67%. Optimization of several factors, including layer thickness, defect density, interface defect density, back metal contact, electron capture cross-section, and absorber bandgap, yielded an enhanced PCE of 30.75% for the optimized FTO/CeO_x/Cs_2TiBr_6/Cu_2O/CuO/Pt PSC. Simplified device architectures were investigated. The simple FTO/CeO_x/Cs_2TiBr_6/Cu_2O/Pt cell delivered a comparable PCE of 30.76%. The HTL-free FTO/CeO_x/Cs_2TiBr_6/Pt design recorded a lower PCE of 22.32%. The optimized Cu_2O/CuO HTL-assisted device exhibited robust thermal performance, with only a modest decrease in PCE (30.99% to 28.16%) with increasing temperature (290 K–400 K). The improved photovoltaic performance of the optimized HTL-assisted devices can be attributed to enhancement in light absorption and carrier generation. An increased built-in field and improved carrier collection also contributed to this improvement. The higher work function of Pt (5.7 eV) formed a better ohmic back contact with the optimized devices, further improving carrier collection.

DOI: 10.46481/asr.2026.5.2.488

Keywords: Cs2TiBr6 perovskite, Perovskite solar cell, Cu2O/CuO, HTL-free perovskite solar cell

Article History:
Received: 22 March 2026
Received in revised form: 21 May 2026
Accepted for publication: 28 May 2026
Available online: 20 July 2026

*Corresponding author Tel. No.: +2348037026581
Email address: emeka.oguzie@futo.edu.ng (E. E. Oguzie)

1. Introduction

Perovskite solar cells (PSCs) have become one of the most promising next-generation photovoltaic technologies because of their exceptional optoelectronic properties, low-cost fabrication process, tunable bandgap, and rapidly increasing power conversion efficiency (PCE) [1–3]. Their ability to effectively convert solar energy into electricity has placed them as viable alternatives to conventional silicon-based photovoltaic devices, which are often associated with expensive synthesis procedures and high energy consumption during manufacturing [4, 5]. In recent years, lead-free halide perovskites such as Cs_2TiBr_6 have gained considerable research attention because they offer improved environmental compatibility, strong thermal stability, and enhanced resistance to moisture-induced degradation compared with lead-based perovskites [3, 6]. Regardless of these advantages, the practical application of Cs_2TiBr_6-based PSCs remains limited by weak optical absorption, high defect density, moderate carrier mobility, and significant charge-carrier recombination losses at interfaces [3, 7]. Moreover, improper energy-level alignment between the absorber and charge transport layers often suppresses carrier extraction efficiency and reduces photovoltaic output. Although previous experimental and theoretical studies have shown appreciable efficiencies for Cs_2TiBr_6 PSCs, the reported performances are still below the theoretical potential of the material system [6, 8–11]. Consequently, there is a strong need to engineer more effective charge transport configurations capable of improving interfacial band alignment, suppressing recombination losses, and improving carrier extraction in order to unlock the full photovoltaic potential of Cs_2TiBr_6-based PSCs.

To address these constraints, this study employs the Solar Cell Capacitance Simulator in one dimension (SCAPS-1D), which is a well-established numerical simulation program widely used for investigating the electrical and photovoltaic characteristics of thin-film solar cells [2, 12]. SCAPS-1D program solves the coupled Poisson equation, electron continuity equation, and hole continuity equation to precisely describe carrier transport, recombination mechanisms, electrostatic potential distribution, and current-voltage behavior within photovoltaic devices. The simulation software is suitable for this study because it allows systematic optimization of material properties, interface parameters, defect densities, and transport-layer configurations without the high cost and complexity associated with experimental fabrication. In this work, CeO_x was selected as the electron transport layer (ETL) because of its wide bandgap, high optical transparency, favorable conduction-band alignment, and low-temperature processability, which collectively boost efficient electron extraction and suppress interfacial recombination [13]. Meanwhile, the Cu_2O/CuO dual hole transport layer (HTL) structure was investigated as an interfacial engineering strategy intended to establish a graded valence-band alignment capable of improving hole selectivity and reducing electron backflow at the rear contact [14–17]. The Cu_2O layer provides efficient hole extraction due to its favorable valence-band alignment and high hole mobility, whereas the CuO layer was introduced to boost work-function matching with the back metal contact [16, 17]. Nonetheless, increasing interface complexity may also introduce additional recombination pathways and transport limitations associated with type-II band alignment if the interfaces are not carefully optimized. Consequently, this study also compares the dual-HTL architecture with simplified single-HTL and HTL-free structures in order to critically evaluate whether the additional interface complexity provides significant photovoltaic benefits.

In this work, a high-performance lead-free Cs_2TiBr_6 perovskite solar cell based on the FTO/CeO_x/Cs_2TiBr_6/Cu_2O/CuO/Au architecture was systematically designed and optimized using SCAPS-1D numerical simulations. The study specifically aimed to improve the photovoltaic performance of Cs_2TiBr_6 PSCs through optimization of absorber thickness, carrier concentration, interface defect density, bulk defect density, electron capture cross-section, absorber bandgap, and back-contact work function. The proposed device operates by improving optical absorption, improving built-in electric-field distribution, suppressing non-radiative recombination, and promoting efficient carrier extraction across the ETL/absorber/HTL interfaces. Following optimization, the proposed PSC achieved a remarkable PCE of 30.75%, with significant improvements in open-circuit voltage (V_{OC}), fill factor (FF), and short-circuit current density (J_{SC}) compared with previously reported Cs_2TiBr_6-based devices. In addition, simplified device architectures involving a single Cu_2O HTL and an HTL-free structure were investigated to evaluate the feasibility of lower-cost and structurally simpler structures. A major limitation of the present study is that the obtained results are based entirely on numerical simulations rather than experimental fabrication. This means that certain assumptions regarding defect states, interface quality, and material uniformity may differ under real laboratory conditions. However, this limitation was proactively addressed by employing experimentally realistic material parameters, and validated SCAPS-1D modeling conditions. Additionally, the optimized parameters adopted in this work, including defect densities, interface trap concentrations, and bandgap tuning ranges, were selected within experimentally realistic limits reported for halide perovskite and oxide transport materials. Comparative analysis with previously published experimental and theoretical studies was also carried out to ensure the physical reliability and practical relevance of the proposed photovoltaic architecture [9, 18–22].

2. Modeling and simulation

The SCAPS-1D package model is designed to simulate semiconductor devices by tackling a trio of fundamental equations: Poisson's equation (1), the electron continuity equation (2), and the hole continuity equation (3). By solving these interconnected partial differential equations, the software determines how electrons and holes are distributed within the electrostatic potential with respect to their position (x). From these calculations, SCAPS-1D can assess important device characteristics, such as short circuit current density (JSC), quantum efficiency (QE), energy band structure, and current-voltage (J-V) behaviour.

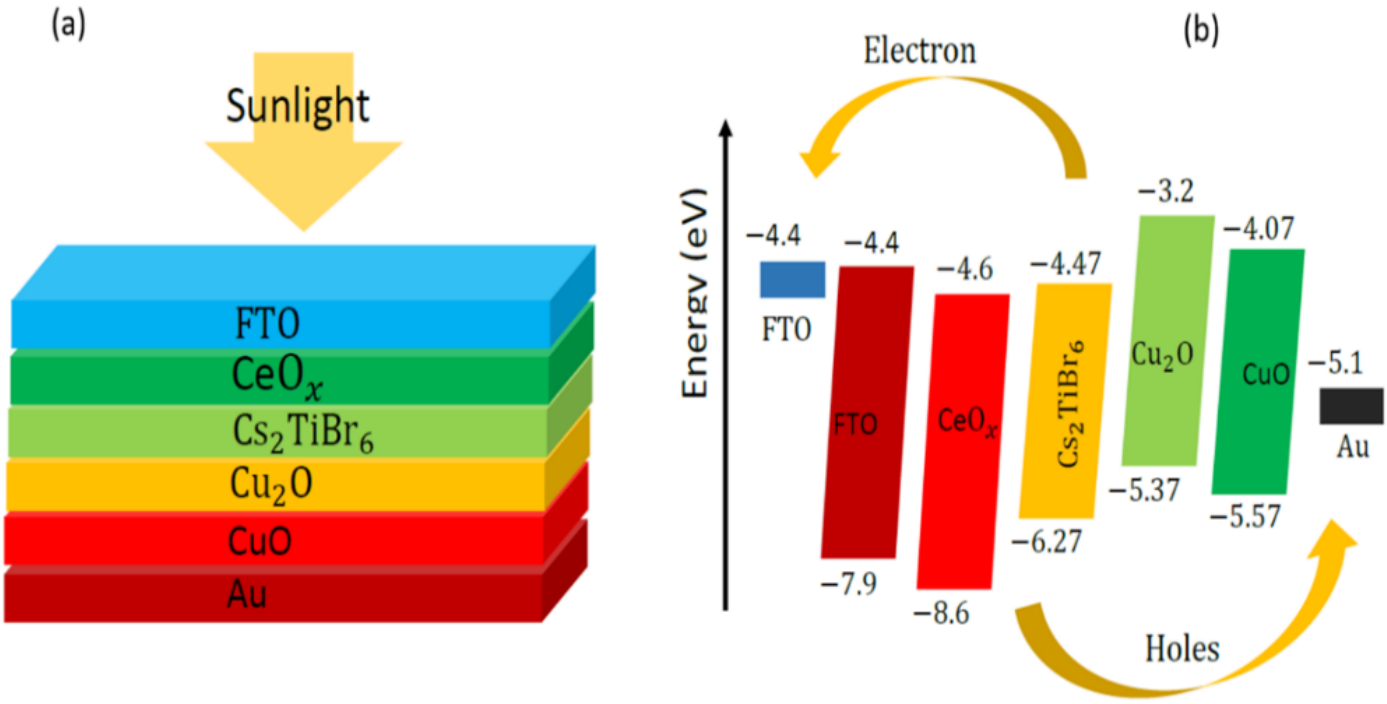

Figure 1: (a) Schematic diagram of the solar cell structure; (b) energy-level diagram.

$$-\frac{\partial}{\partial x}\left(U\frac{\partial V}{\partial x}\right) = q\left[p(x) - n(x) + N_D^+(x) - N_A^-(x) + p_t(x) - n_t(x)\right], \tag{1}$$

$$\frac{\partial n}{\partial t} = \frac{1}{q}W_1 + G_n - R_n, \tag{2}$$

$$\frac{\partial p}{\partial t} = \frac{1}{q}W_2 + G_p - R_p, \tag{3}$$

where U= εx, $W_1 = \frac{\partial J_n}{\partial x}$ and $W_2 = \frac{\partial J_p}{\partial x}$, ε is dielectric permittivity, V is potential, q is charge, $p(x)$ is free holes concentration, $n(x)$ is free electrons concentration, $N_A^-(x)$ is acceptor carrier density, $N_D^+(x)$ is donor carrier density, $p_t(x)$ is trap density of hole, J_n is current density of electron, $n_t(x)$ is trap density of electron, J_p is current density of holes, R_p is recombination rate of hole, R_n is recombination rate of electron, G_p is holes generation rate, and G_n is electrons generation rate.

2.1. Device structure and input parameters

The device structure and corresponding energy band diagram are depicted in Figure 1, while Table 1 showcases the fundamental physical parameters of the materials, drawn from various relevant published studies [3, 14, 15, 23]. The goal of this research is to investigate the double-HTL PSC configured as FTO/CeO_x/Cs_2TiBr_6/Cu_2O/CuO/Au. To bolster our rationale for choosing the double-HTL device, we also simulated the single-HTL counterparts (FTO/CeO_x/Cs_2TiBr_6/Cu_2O/Au and FTO/CeO_x/Cs_2TiBr_6/CuO/Au). The Cu_2O-based and CuO-based single-HTL devices may face challenges due to a relatively high defect density at the interfaces, which can lead to charge recombination. On the other hand, employing the double HTL (Cu_2O/CuO) facilitates a graded, stepwise energy-level alignment, which improves hole extraction, reduces recombination losses, and enhances stability compared to using either Cu_2O or CuO on their own. Although the Cu_2O/CuO bilayer may boost band selectivity and work-function alignment, the additional interface can also introduce recombination losses and carrier-transfer limitations linked with type-II band alignment. Therefore, comparative simulations comprising single-HTL and HTL-free structures were additionally carried out to determine whether the dual HTL configuration offers meaningful photovoltaic advantages after optimization.

Table 2 presents parameters for the interface layer. The work functions for FTO and Au are 4.4 eV and 5.1 eV, respectively [2, 24]. The simulations were conducted under AM 1.5G illumination, with an incident light power density of 1000 W/m^2 at a frequency of 1×10^6 Hz, a scan voltage range from 0 to 1.5 V, and an operating temperature of 300 K. To find the best parameters

Table 1: Simulation parameters for the single-junction solar cell.

Parameter	FTO	CeO_x	Cs_2TiBr_6	Cu_2O	CuO
Thickness (μm)	0.5	0.1	0.5	0.6	0.6
E_g (eV)	3.5	3.5	1.8	2.2	1.51
χ (eV)	4.3	4.4	4.47	3.5	4.07
ε_r	9.0	9.0	10	7.5	18.1
N_C (cm^{-3})	2.2×10^{18}	1.0×10^{20}	6.0×10^{19}	2.0×10^{19}	2.2×10^{19}
N_V (cm^{-3})	1.8×10^{19}	2.0×10^{21}	2.0×10^{19}	1.0×10^{19}	5.5×10^{20}
μ_n ($cm^2\ V^{-1}\ s^{-1}$)	200	100	4.4	200	100
μ_p ($cm^2\ V^{-1}\ s^{-1}$)	10	25	2.5	8600	0.1
eV_{th} (cm/s)	1×10^7	1×10^7	1×10^7	1×10^7	1×10^7
hV_{th} (cm/s)	1×10^7	1×10^7	1×10^7	1×10^7	1×10^7
N_D (cm^{-3})	2×10^{19}	1×10^{18}	0	0	0
N_A (cm^{-3})	0	0	1×10^{14}	1×10^{16}	1×10^{18}
N_t (cm^{-3})	1×10^{15}	1×10^{15}	1×10^{14}	1×10^{15}	2.5×10^{14}
$\sigma(e)$ (cm^2)	1×10^{-15}	1×10^{-15}	1×10^{-15}	1×10^{-15}	1×10^{-15}
$\sigma(h)$ (cm^2)	1×10^{-15}	1×10^{-15}	1×10^{-15}	1×10^{-15}	1×10^{-15}

Table 2: Interface defect parameters.

Parameter	CeO_x/Cs_2TiBr_6	Cs_2TiBr_6/Cu_2O	Cu_2O/CuO
$\sigma(e)$ (cm^2)	1×10^{-15}	1×10^{-15}	1×10^{-15}
$\sigma(h)$ (cm^2)	1×10^{-15}	1×10^{-15}	1×10^{-15}
Energetic distribution	Single	Single	Single
Energy level with respect to E_V (eV)	0.60	0.60	0.60
Characteristic energy (eV)	0.10	0.10	0.10
Interface defect density (cm^{-2})	1×10^{13}	1×10^{13}	1×10^{13}

for improving device performance, we varied the thickness of all layers, the defects in the absorber, all interface defects, the electron cross-section, and the series resistance of the prototype device.

3. Results and discussion

Figure 2 presents the equilibrium energy band profiles of the three prototype device configurations, illustrating the conduction band edge (E_C), valence band edge (E_V), and the corresponding electron and hole quasi-Fermi levels (F_n and F_p) across the device thickness. These diagrams provide critical insights into how charge carriers are extracted and how recombination characteristics affect the photovoltaic performance of each device structure. For Figure 2a, where Cu_2O is the only HTL, a favorable alignment of the valence bands between Cu_2O and Cs_2TiBr_6 could be observed. This promoted efficient hole transfer to the rear electrode. The substantial conduction-band offset at this interface successfully prevented electron back-flow, and reduced interfacial recombination [25], suggesting the potential for a higher V_{OC}. Nevertheless, this energy barrier also creates a moderate resistance to hole transport, which could be seen in the intermediate FF observed for this architecture.

Figure 2b demonstrated a different behavior for the CuO-sole HTL structure. CuO boosts optical absorption due to its smaller bandgap, but the band diagram showed a significant conduction-band spike located at the Cs_2TiBr_6/CuO interface. This sharp, energetic discontinuity led to electron accumulation and promoted interfacial recombination [25], which reduced the charge extraction efficiency. Therefore, this structure might exhibit a noticeably lower V_{OC} and PCE values compared to the Cu_2O-assisted cell, even though it recorded a slightly higher J_{SC}.

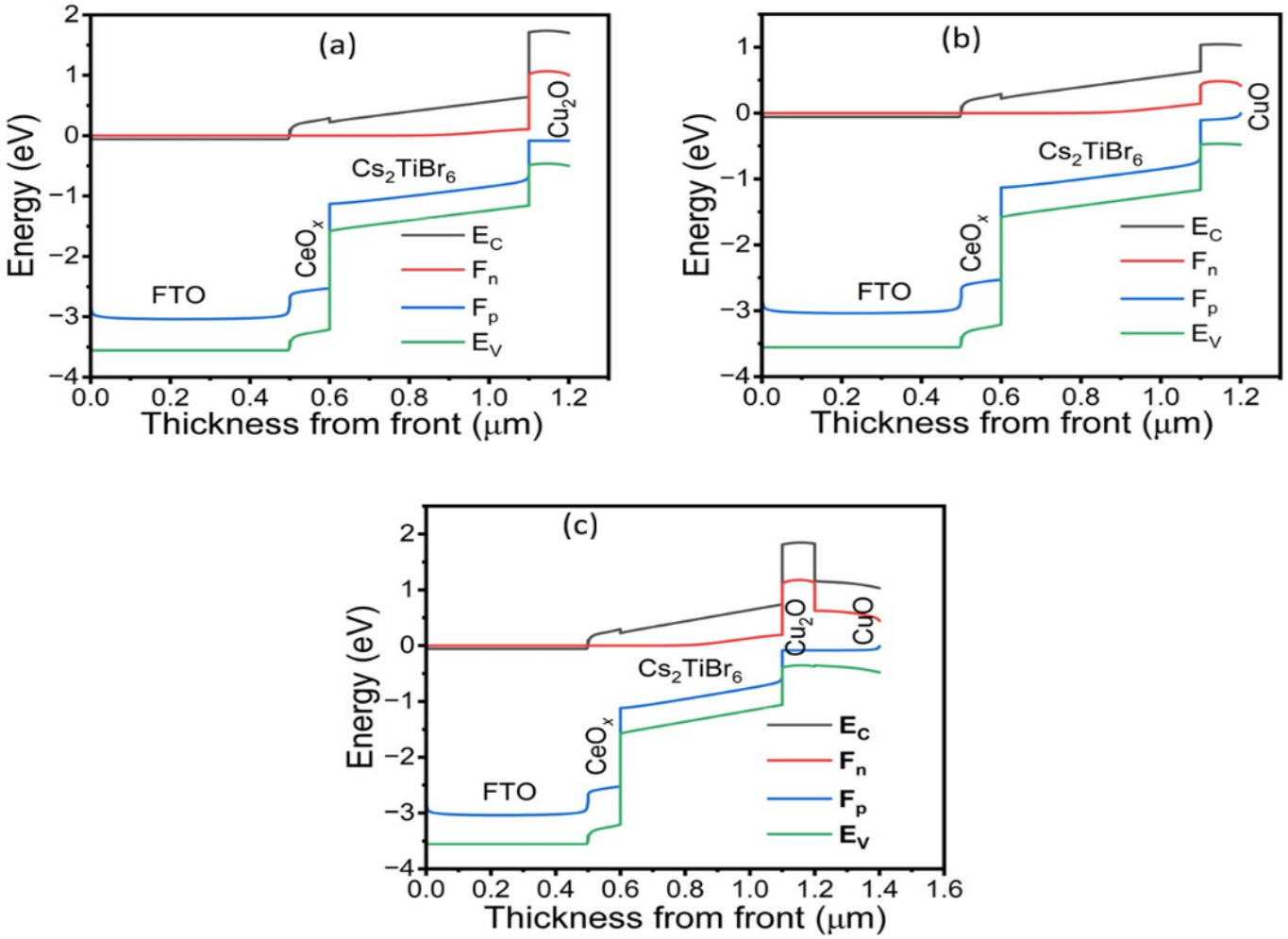

Figure 2: Energy band for the (a) Cu_2O-based PSC, (b) CuO-based PSC, and (c) Cu_2O/CuO-assisted PSC.

Table 3: Correlation between photovoltaic performance of the prototype PSCs.

Solar cell	V_{OC} (V)	J_{SC} (mA/cm^2)	FF (%)	PCE (%)
FTO/CeO_x/Cs_2TiBr_6/Cu_2O/Au	0.76	16.55	65.97	8.33
FTO/CeO_x/Cs_2TiBr_6/CuO/Au	0.62	18.26	60.62	6.91
FTO/CeO_x/Cs_2TiBr_6/Cu_2O/CuO/Au	0.72	16.57	72.48	8.67

Figure 2c shows the bilayer HTL architecture, featuring Cu_2O/CuO as dual HTL that exhibit the best energy-level alignment. This gradual cascade in the valence band allowed for smooth hole transport, whereas the positioning of the conduction band effectively blocked electrons. Recombination losses were reduced at rear interface, and was further enhanced by this internal field [25]. Consequently, this architecture achieved the highest values of FF and PCE compared to the two other prototype cells. Nonetheless, despite the favorable graded valence-band structure, the additional Cu_2O/CuO interface may also contribute to interfacial carrier-transfer resistance and trap-assisted recombination if not properly optimized. This has motivated further investigation of simplified single-HTL architectures.

Table 3 presents the photovoltaic performance of the three prototype Cs_2TiBr_6-based PSC configurations that employed different HTL structures. Combining and changing CuO and Cu_2O as the HTLs resulted in substantial differences in the values of PCE, J_{SC}, V_{OC}, and FF. These variations explain why HTL selection is essential, and reveal how they influence other features such as carrier extraction, interfacial recombination, and the output of the PSC.

The FTO/CeO_x/Cs_2TiBr_6/Cu_2O/Au PSC recorded PCE of 8.33%. This performance could be traced to its relatively high V_{OC} value of 0.76 V and a competitive J_{SC} value of 16.55 mA/cm^2. The p-Cu_2O layer exhibits good valence band alignment with Cs_2TiBr_6 and boasts an impressive hole mobility of 8600 cm^2/Vs, which facilitates the rapid extraction and transport of holes. The high value

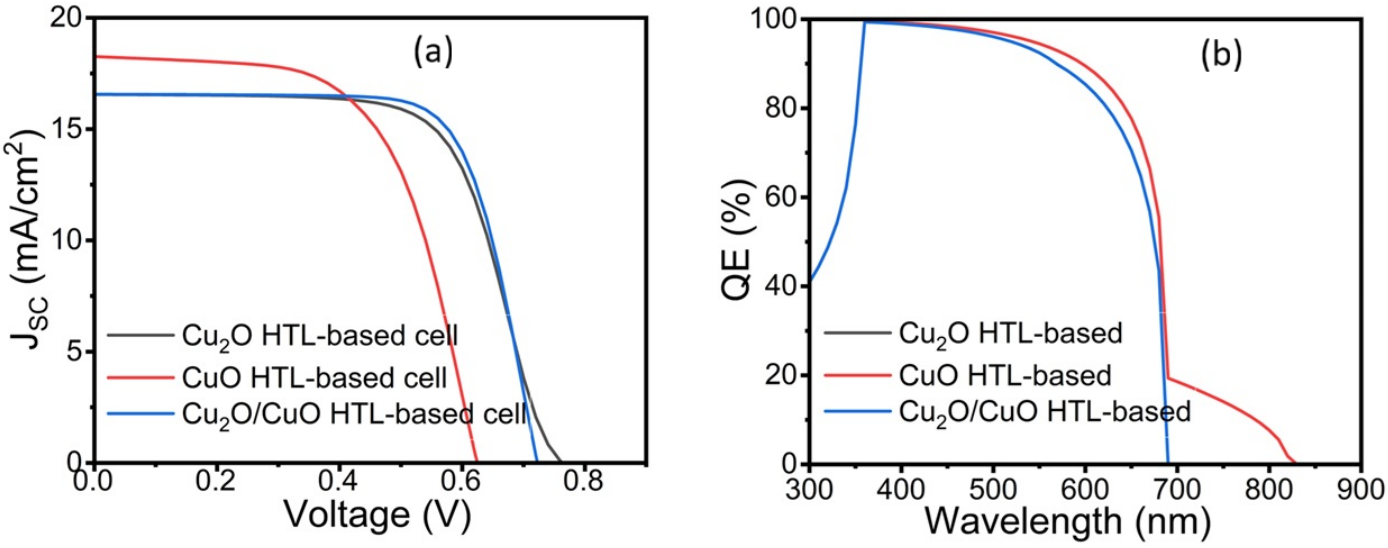

Figure 3: Graph of (a) J_{SC} versus voltage for the prototype Cs_2TiBr_6-based PSCs using various HTLs. (b) QE versus wavelength.

of V_{OC} observed in this PSC indicates that interfacial recombination was reduced, thanks to the significant electron energy barrier at the Cs_2TiBr_6/Cu_2O heterointerface that blocked electron leakage into the HTL. As a result, the Cu_2O-based device demonstrated effective charge separation and effective photovoltage generation. Nevertheless, the FF was moderate at 65.97%, indicating some resistive losses that can be associated with trap states in the Cu_2O HTL or uneven charge collection across the PSC.

Employing CuO HTL in the place of Cu_2O in the second cell (FTO/CeO_x/Cs_2TiBr_6/CuO/Au) resulted in a drop in PCE to 6.91%. This decrease was due to a lower V_{OC} of 0.62 V and a FF value of 60.62%, although there was a small uptick in J_{SC} (18.26 mA/cm^2). The increase J_{SC} could be ascribed to CuO's smaller bandgap (1.51 eV), which improved photon absorption at longer wavelengths and promoted the density of photogenerated carriers near the back contact. Nevertheless, CuO HTL struggles with poor hole mobility (μ_p = 0.1 cm^2/Vs), leading to substantial resistive losses and escalated recombination at the Cs_2TiBr_6/CuO interface. The lower V_{OC} value suggests greater non-radiative recombination losses, likely emanating from a rise in defect-interface density and poor band alignment. These factors hindered charge transport dynamics and impacted the PCE of the device.

The device employing a double HTL (FTO/CeO_x/Cs_2TiBr_6/Cu_2O/CuO/Au) demonstrated impressive output and recorded a PCE of 8.67%. It exhibited a V_{OC} of 0.72 V, a J_{SC} of 16.57 mA/cm^2, and a significantly enhanced FF value of 72.48%. This improved performance could be ascribed to the complementary functions of the HTLs: (i) The Cu_2O layer next to Cs_2TiBr_6 promoted efficient hole extraction and reduced recombination by ensuring better valence-band alignment and larger hole mobility. (ii) The incorporation of CuO near the Au contact improved hole selectivity and minimized back-carrier reflection, thanks to its favourable work-function alignment with the Au metal contact.

The cascade-type band structure formed a well-ordered built-in potential drop across the HTL, which assisted in minimizing interfacial charge buildup and reducing the series resistance. The significant enhancement in FF explains the decreased energy-loss pathways and improved transport uniformity which is enabled by the bilayer design. These results suggest that HTLs can be successfully engineered to improve the stability and efficiency of lead-free solar cells.

Figure 3b illustrates a comparison of QE results of the three PSCs. The salient differences across the visible to near-infrared spectrum directly relate to the changes in the values of J_{SC} shown in Figure 3a and Table 3. The Cu_2O/CuO bilayer and Cu_2O-based PSCs illustrated broad and enhanced QE responses in the wavelength range of 350–700 nm, indicating the good use of incoming photons to generate carriers. This strong response is consistent with their higher J_{SC} values of 16.57 and 16.55 mA/cm^2, respectively. In contrast, the CuO HTL-free PSC exhibited a relatively higher magnitude of QE in most of the visible spectrum and even extended its spectral response to longer wavelengths, up to 820 nm compared with the others. This broad absorption range is due to the CuO HTL's narrow bandgap (1.51 eV), which improved its ability to capture long-wavelength photons. This enlarged spectral activity explains the CuO-based device's highest J_{SC} value, although its carrier extraction efficiency was less than that of the other two PSCs.

3.1. Impact of CeO_x ETL thickness on device performance

CeO_x ETL was varied from 0.10 to 1.00 μm in thickness to evaluate its influence on device output. The corresponding PV results in Figure 4 confirmed that the variations in CeO_x thickness exerted negligible influence on all key performance parameters. The device maintained a stable V_{OC} value of 0.72 V, J_{SC} of 16.55–16.57 mA/cm^2, FF value of 72.47% and PCE of 8.67%.

The insignificant impact of thickness is primarily attributed to the wide bandgap and high optical transparency of CeO_x in the visible spectral region which is relevant for uninterrupted light absorption in the Cs_2TiBr_6 absorber. The increasing ETL thickness

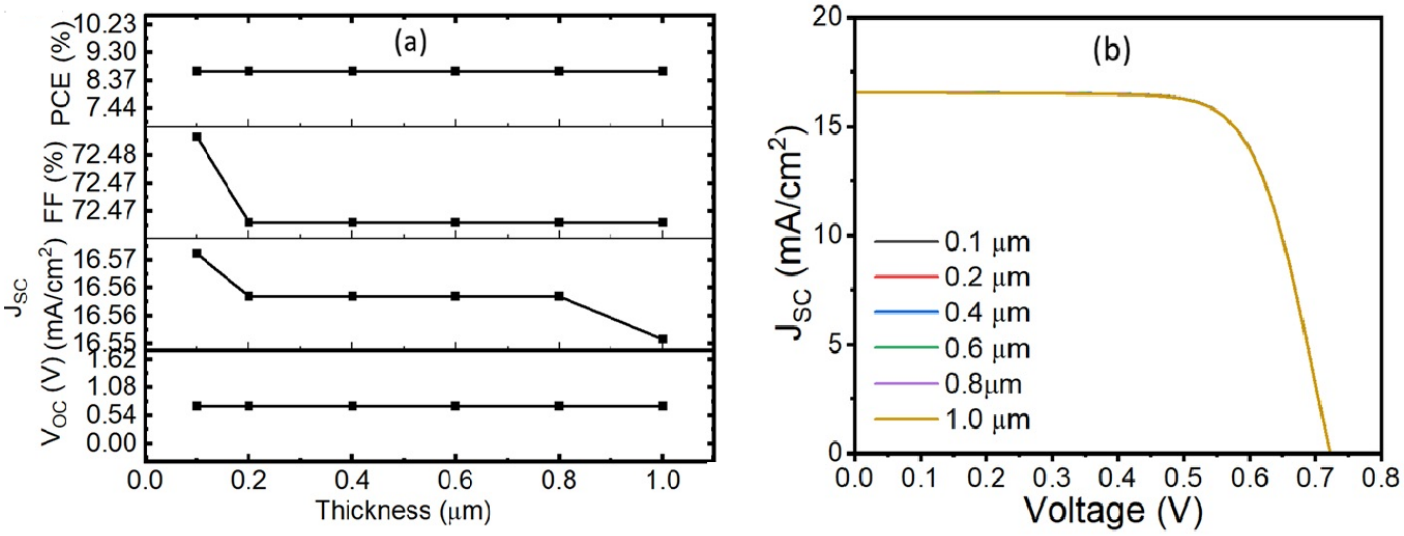

Figure 4: (a) Variation of V_{OC}, J_{SC}, FF, and PCE with CeO_x layer thickness, (b) Associated J-V curves.

did not introduce additional light absorption, so the photon flux reaching the perovskite absorber remained unchanged, resulting in a constant J_{SC}. Furthermore, the electronic properties of CeO_x, including its conduction band alignment with Cs_2TiBr_6 and adequate electron mobility, ensure effective charge extraction even at increased thickness. Consequently, series resistance did not increase, preserving both FF and PCE.

It could also be assumed that the operation of this device was interface-dominated, rather than bulk-transport-limited. Because the band offsets and interface defect density at the CeO_x/Cs_2TiBr_6 interface remained constant with thickness, the recombination dynamics were unaffected, leading to the uniform V_{OC}.

3.2. Impact of varied perovskite absorber thickness

The effect of Cs_2TiBr_6 absorber layer thickness on photovoltaic performance was examined by varying the thickness from 0.40 to 1.40 μm. Figure 5 demonstrates how both the generation of J_{SC} and the FF depend on the thickness of the absorber. Interestingly, the V_{OC} stayed fixed at around 0.72–0.73 V. As the thickness increased, J_{SC} rose from 15.66 to 18.61 mA/cm^2 with an increase in thickness from 0.40 to 1.40 μm. This boost could be attributed to better light absorption (as seen in Figure 5b) and improved optical confinement with greater thickness which allowed more incoming photons to generate electron-hole pairs in the active layer. This degradation could be associated with longer transport pathways and increased bulk recombination probability for electron-hole pairs in the active layer. As Cs_2TiBr_6 has a direct bandgap of approximately 1.8 eV, thicker films allowed deeper penetration of short- and mid-visible photons, thereby increasing the number of collected charge carriers.

However, the FF exhibited the opposite behaviour. As thickness increased beyond 1.0 μm, the FF gradually declined from 72.66 to 67.67%. This degradation could be associated with longer transport pathways and increased bulk recombination probability [12, 26]. In thicker perovskite films, photogenerated carriers must traverse larger distances before reaching their respective charge-selective layers, which heightened the susceptibility to trap-assisted recombination, particularly when defect density is not minimized. The increase in series resistance at larger thickness further contributed to the reduction in FF. As a result of the competing influences of enhanced optical absorption (increasing J_{SC}) and aggravated transport limitations (reducing FF), the PCE followed a rise-and-fall behavior. The maximum PCE of 9.37% occurs at 1.00 μm, indicating that this thickness provided a suitable balance between photon harvesting and effective charge extraction. Further increase beyond this thickness led to a minor decline in PCE due to the reduction in FF that overpowered the modest increase in J_{SC}.

3.3. Influence of varied Cu_2O HTL thickness

To elucidate the impact of the primary HTL on charge-carrier dynamics, the thickness of the Cu_2O layer in the prototype $FTO/CeO_x/Cs_2TiBr_6/Cu_2O/CuO/Au$ device was varied from 0.1 to 1.0 μm. The photovoltaic parameters presented in Figure 6 demonstrates a positive but gradual improvement in device performance with increasing Cu_2O thickness. The V_{OC} increased negligibly from 0.72 to 0.73 V, indicating reduced recombination at the Cs_2TiBr_6/Cu_2O interface as the Cu_2O layer becomes sufficiently thick to provide improved electronic selectivity and contact uniformity. A more noticeable improvement could be seen in the FF, which increased from 72.48 to 74.0% as the film thickened (0.40–1.0 μm). Both series resistance and interfacial barrier effects were reduced once the Cu_2O layer achieved a sufficient thickness [27] based on this enhancement, allowing for complete coverage and better pathways for hole transport. Similarly, the J_{SC} gradually rose from 16.56 to 16.79 mA/cm^2 due to improved hole extraction

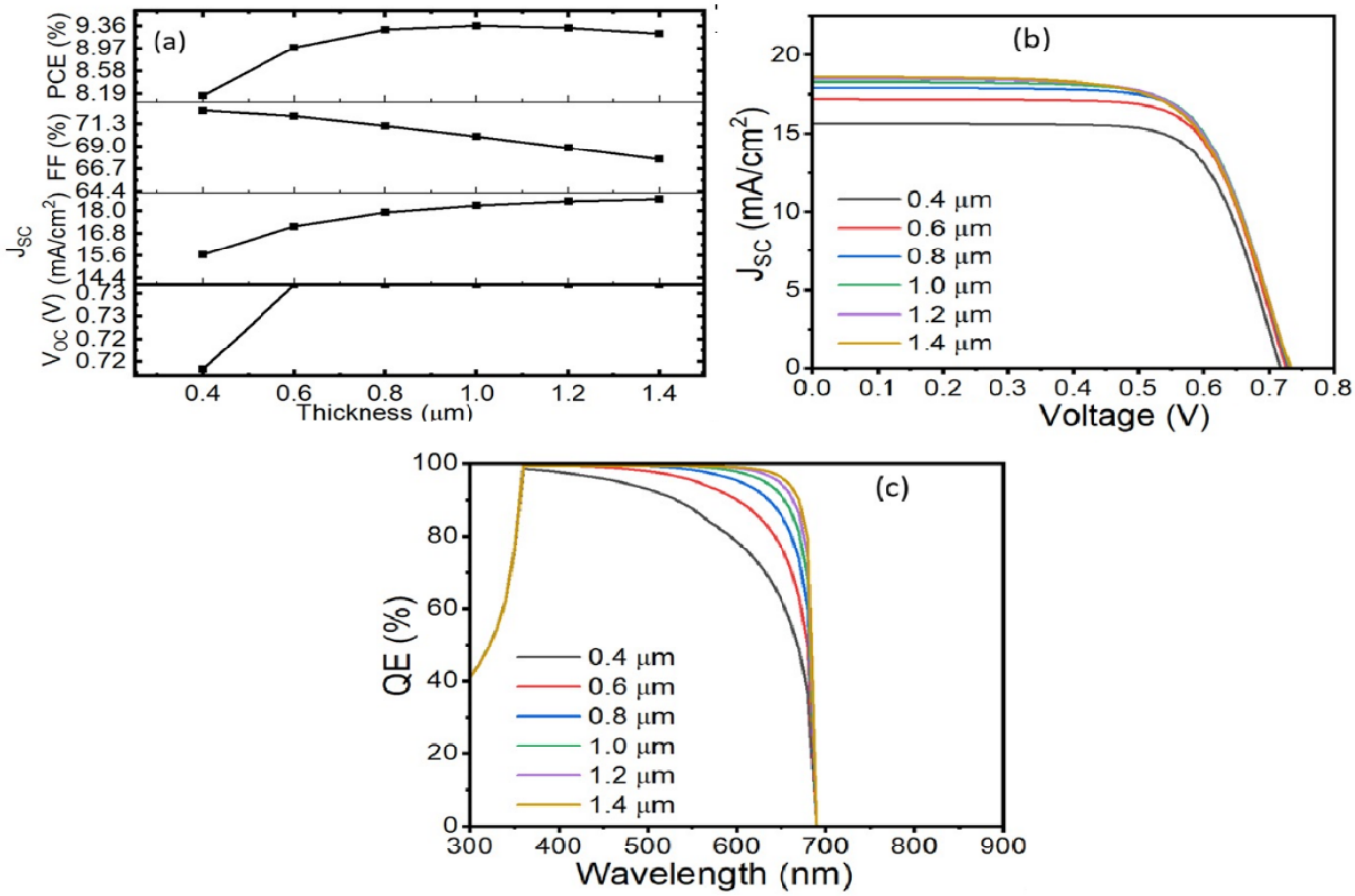

Figure 5: Variation of V_{OC}, J_{SC}, FF, and PCE with Cs_2TiBr_6 layer thickness, (b) Associated J-V curves, (c) QE plots.

and reduced space-charge buildup at the interface of Cs_2TiBr_6/Cu_2O. Although the Cu_2O HTL is not a strong optical absorber, its favorable energy band alignment significantly enhances carrier extraction. The thickness layer assisted to cushion the built-in electric field and improved the likelihood of carrier collection throughout the PSC. The combined effect of these small improvements in the values of V_{OC}, J_{SC} and FF resulted in an increase in PCE from 8.67 to 9.03%, although the benefits started to dwindle beyond a thickness of 0.60 μm. This shows that once the Cu_2O film reached a reasonable thickness to ensure complete substrate coverage, adding more thickness had insignificant improvement on carrier extraction, and only slightly affected the resistive losses.

These results suggest that the device operated efficiently during transport and did not face major recombination problems for Cu_2O layer thicknesses in the range of 0.40 to 1.0 μm. The range of 0.60 to 0.80 μm emerged as the most advantageous, balancing both performance and ease of fabrication.

Thinner films (<0.20 μm), while still functional, may suffer from incomplete substrate coverage or higher interfacial recombination rates, leading to slightly lower FF and PCE.

3.4. Influence of varied CuO HTL thickness

Figure 6 showed that varying the CuO thickness from 0.1 – 1.0 μm produced a monotonic decline in V_{OC} from 0.74 – 0.70 V, near-constant J_{SC} of 16.56–16.57 mA/cm^2, and an FF that first improved (71.20 – 72.80%) from 0.1 – 0.4 μm, and then degraded (72.66 – 72.27%) from 0.6–1.0 μm. Therefore, PCE attained the highest value of 8.67% at thin CuO (0.1 – 0.2 μm) and progressively dropped to 8.36% at 1.0 μm. The CuO served as the hole-selective capping layer adjacent to Au, aiding work-function matching and back-contact selectivity. However, CuO's low hole mobility (0.1 $cm^2V^{-1}s^{-1}$) means that increasing its thickness primarily adds series resistance and increases the chance of bulk and interfacial trap-assisted recombination [26, 27]. The observed V_{OC} loss with thickness was consistent with greater non-radiative recombination and a reduced quasi-Fermi-level splitting in the absorber/HTL stack. The initial FF rise from 0.10 to 0.20 – 0.40 μm reflected improved film continuity and contact uniformity (suppression of local shunting and contact inhomogeneity at very thin CuO). Beyond 0.4 μm, transport penalties dominated to lower FF and PCE. During practical design, for the Cu_2O/CuO cascade, CuO should be kept thin (between 0.1 and 0.2 μm) to preserve the beneficial selectivity/work-function alignment while avoiding resistive and recombination penalties.

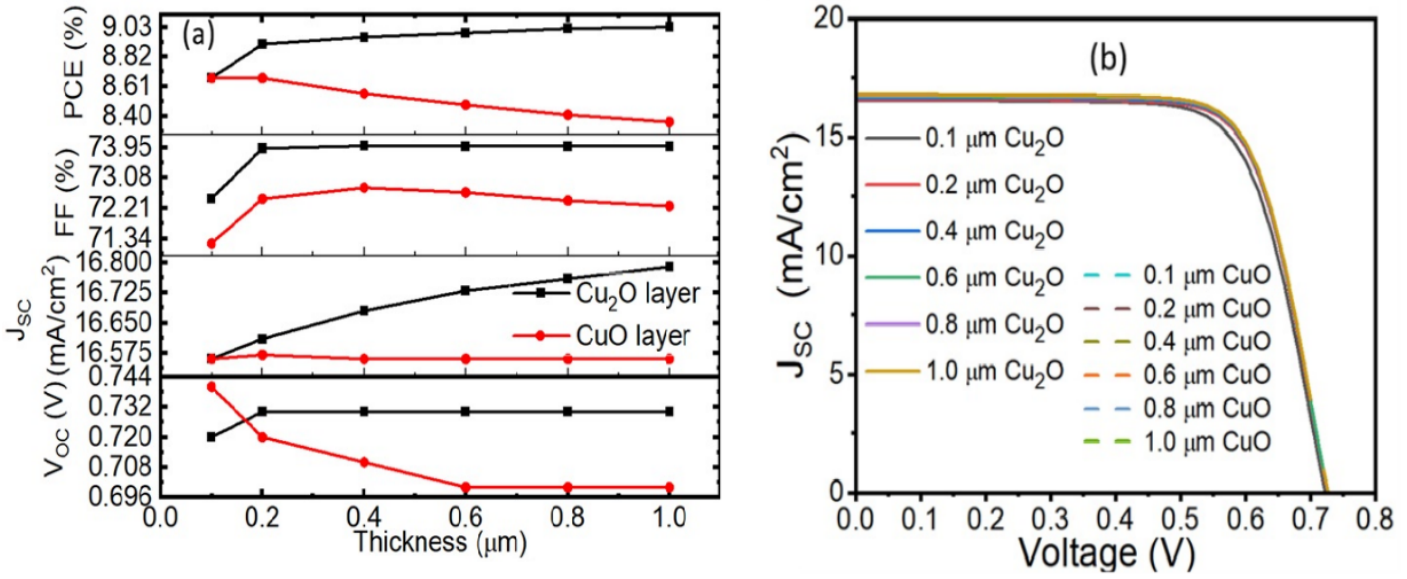

Figure 6: (a) Variation of V_{oc}, J_{sc}, FF, and PCE with thickness of Cu_2O and CuO layers, (b) J–V curves for Cu_2O and CuO layers.

Table 4: Impact of acceptor carrier concentration on photovoltaic parameters.

Carrier concentration (cm^{-3})	V_{OC} (V)	J_{SC} (mA/cm^2)	FF (%)	PCE (%)
10^{14}	0.72	16.59	70.01	8.33
10^{15}	0.72	16.58	69.61	8.28
10^{16}	0.72	16.56	72.48	8.67
10^{17}	–	16.56	–	9.80
10^{18}	–	16.56	–	10.76

3.5. Influence of carrier concentration of the Cu_2O layer

Table 4 and Figure 7 reveal that increasing the carrier concentration (10^{14}–10^{18} cm^{-3}) of the Cu_2O HTL improved the PSC performance mainly through better hole extraction, lower series resistance, and sturdy interfacial band bending. The V_{OC} remained constant, whereas changes in J_{SC} were small. But the FF increased significantly, causing a substantial rise in PCE. The PCE continues to increase to 9.80% and 10.76% as the doping concentration increased to 10^{17} and 10^{18} cm^{-3}, while J_{SC} remained constant at 16.56 mA/cm^2. This showed that the primary benefit of Cu_2O doping is the improvement of conductivity and charge collection.

The conductivity in the HTL can be described by Equation (4) [27]. Since Cu_2O is a p-type HTL, the conductivity is mainly controlled by holes, according to Equation (5) [27].

$$\sigma = q\left(\mu_p p + \mu_n n\right), \tag{4}$$

$$\sigma = q\mu_p p, \tag{5}$$

where σ represents the electrical conductivity. An increase in carrier concentration led to an improvement in conductivity [27], which decreased the resistive loss in the HTL. A higher hole concentration reduced bulk series resistance, which improves the squareness of the J-V curve and therefore raised the FF. This supported the improvement in FF with an increase in the Cu_2O carrier concentration.

The improvement can also be explained from the built-in potential across the junction. For a p-n heterojunction, which can be expressed as in Equation (6) [27].

$$V_{bi} = \frac{kT}{q} \ln \frac{N_A N_D}{n_i^2}, \tag{6}$$

where N_A denotes the acceptor concentration in Cu_2O, N_D represents the donor concentration in the adjacent n-type region, k is Boltzmann constant, T is temperature, and q is electron charge. Increasing the acceptor concentration shifted the Cu_2O Fermi level

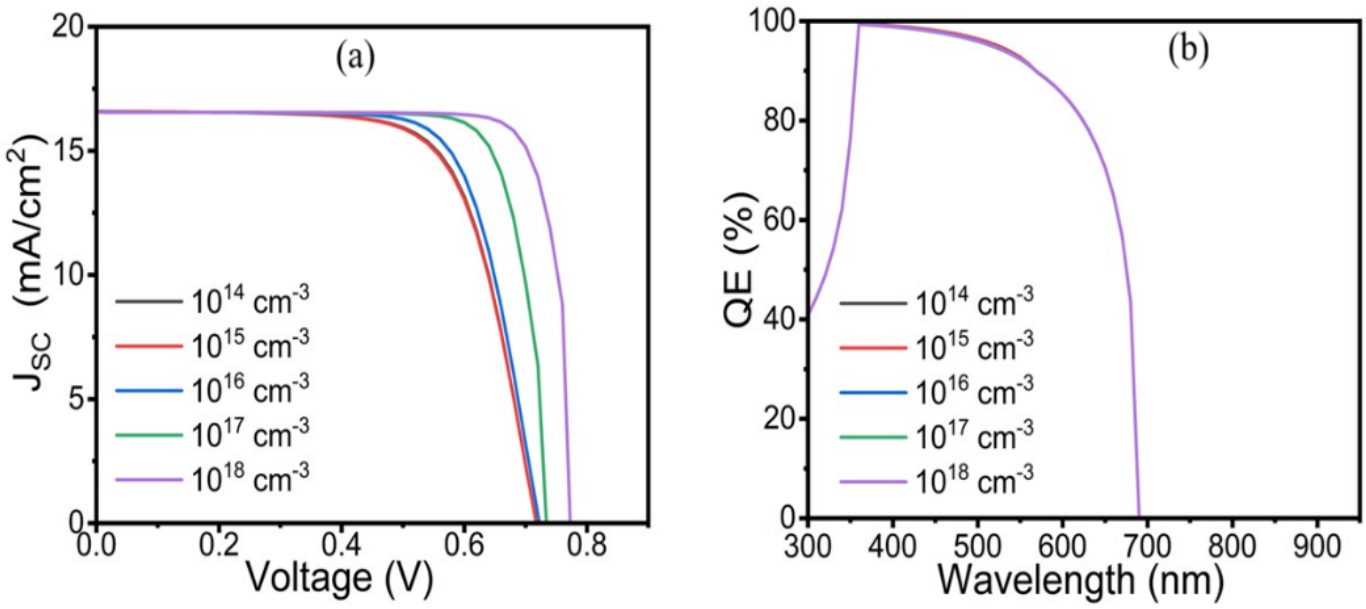

Figure 7: J-V curves for the impact of acceptor carrier concentration, (b) QE plots.

closer to the valence band and strengthened the built-in electric field near the absorber/Cu_2O interface. This favoured hole extraction from the absorber into Cu_2O layer and suppressed interfacial carrier accumulation, thereby reducing recombination losses.

The V_{OC} can be described by Equation (7) [28].

$$V_{OC} = \frac{nkT}{q} \ln\left(\frac{J_{ph}}{J_0} + 1\right), \tag{7}$$

where J_{ph} is the photogenerated current, J_0 the dark saturation current, and n is the ideality factor.

The increased PCE could be ascribed to the reduction in recombination-related losses and better diode quality, which effectively lowered J_0, since V_{OC} remained constant, and J_{SC} improved only slightly. Even though V_{OC} was not listed up to the 10^{17} cm^{-3} doping level, the remarkable increase in PCE after this doping level implied that the product of $V_{OC}\times FF\times J_{SC}$ continued to grow significantly larger at higher doping. The PCE can be expressed by Equation (8) [29].

$$\eta = \frac{V_{OC} J_{SC} FF}{P_{in}}. \tag{8}$$

3.6. Defect density impact of the CeO_x ETL

The effect of the CeO_x ETL bulk defect density was evaluated over five orders of magnitude (10^{11}-10^{16} cm^{-3}) as shown in Figure 8. All key figures of merit remained effectively invariant: V_{OC}, J_{SC}, FF, and PCE being 0.72 V, 16.56 mA/cm^2, 72.48%, and 8.67%, respectively. This performance suggested that the ETL was largely tolerant to a wide range of bulk defect density.

Moreover, V_{OC} was set primarily by recombination in the absorber and interfaces, not by losses inside a transparent, moderately doped ETL. The CeO_x/Cs_2TiBr_6 interface defect density remained fixed at 10^{13}cm^{-2}, and band offsets were constant therefore, the quasi-Fermi-level splitting and the resulting V_{OC} did not change with CeO_x bulk defect density. The flat FF similarly reflects unchanged series resistance and unchanged barrier heights. Defect density did not affect the optical transparency of the CeO_x thereby, keeping the absorption unaffected and hence the steady J_{SC}.

3.7. Defect density impact of the absorber

To investigate the sensitivity of the absorber quality to device efficiency, the bulk defect density of the Cs_2TiBr_6 layer was varied from 10^{11} to 10^{16} cm^{-3}. The results in Figure 8 revealed three distinct performance regimes. At low defect levels (10^{11}-10^{13} cm^{-3}), the performance remained essentially unchanged with a stable V_{OC} of 0.72 V, J_{SC} of 16.57 mAcm^2, FF of 73.00%, and a maximum PCE of 8.76%. This uniformity in the PV parameters indicates that carrier recombination in the perovskite absorber was low and that charge extraction remained highly efficient within the investigated defect trap range. A significant deterioration of device performance began at defect density of 10^{14} cm^{-3} due to decrease in FF (73.0–72.48%). Although the values of V_{OC} and J_{SC} remained nearly unchanged at this stage, the onset of increased non-radiative recombination suggested a decline in carrier transport uniformity and a decrease in the internal electric field strength within the perovskite absorber layer.

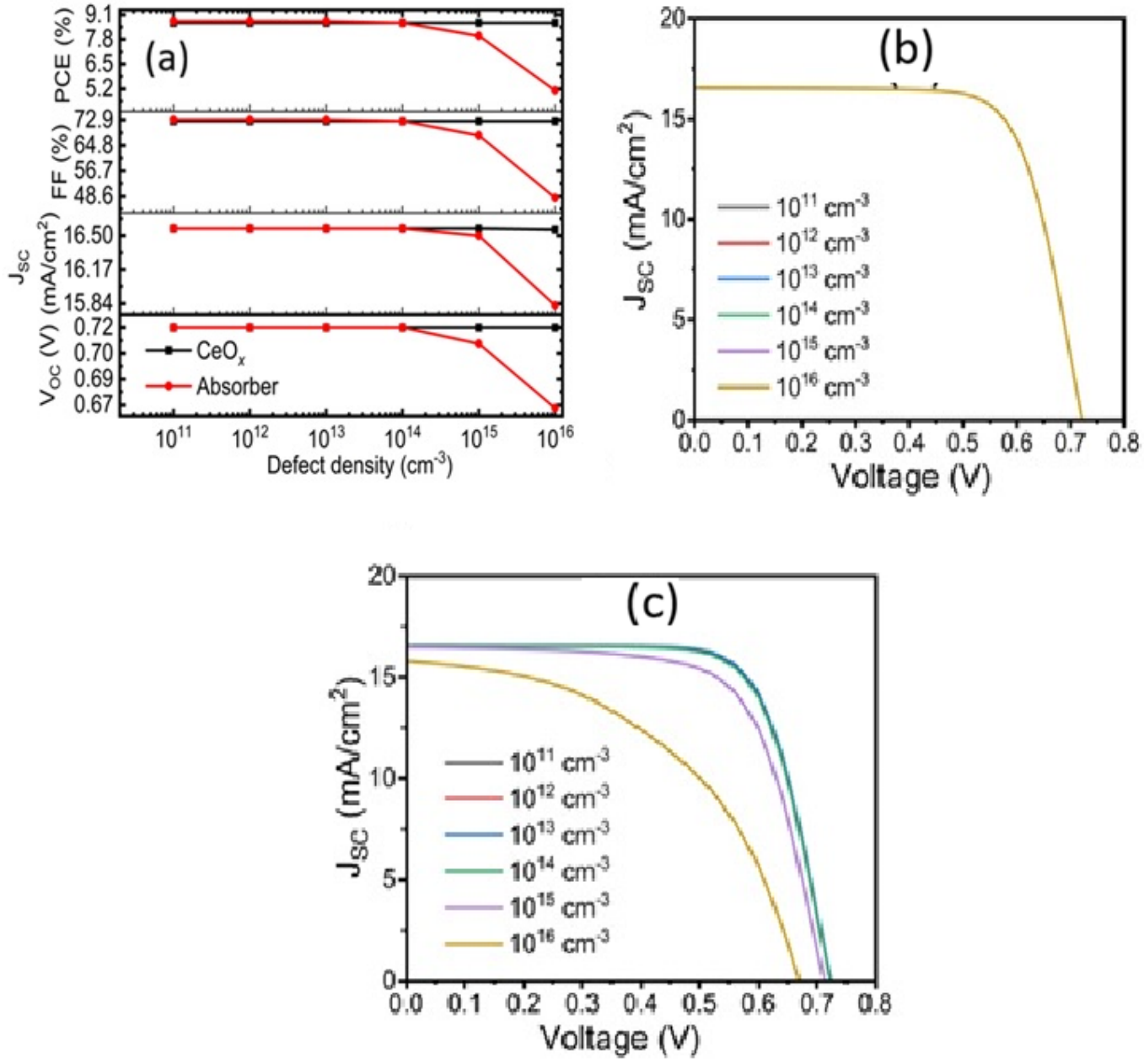

Figure 8: Dependence of V_{OC}, J_{SC}, FF, and PCE on bulk defect density of CeO_x ETL and absorber layer, (b) Associated J-V curves.

A sharp performance degradation occurred when the defect traps reached 10^{15}-10^{16} cm^{-3}. The device PCE significantly decreased from 8.76 to 5.11%, accompanied by a severe drop in both V_{OC} (0.72 - 0.67 V) and FF (73.0 - 48.10%). The diminished quasi-Fermi level splitting at high defect densities indicated strong Shockley–Read–Hall (SRH) recombination, shortening the carrier lifetime and reducing the effective diffusion length to below the absorber thickness. As a result, photogenerated carriers failed to reach the charge transport layers, leading to the observed decline in J_{SC} and FF.

The defect density of the HLTs (Cu_2O and CuO) were not investigated because they produced no effects on device performance, suggesting a wide range of tolerance to defect-induced recombination.

3.8. Interface defect density impact of the CeO_x/absorber

The influence of the CeO_x/Cs_2TiBr_6 interface quality on device performance was investigated by varying the defect density at the CeO_x/Cs_2TiBr_6 interface in the range 10^{10} - 10^{15} cm^{-2}. The photovoltaic parameters depicted in Figure 9 indicated that all metric parameters remained unchanged, with constant values: V_{OC}, J_{SC}, FF and PCE of 0.72 V, 16.56 mA/cm^2, 72.48%, and 8.67%,

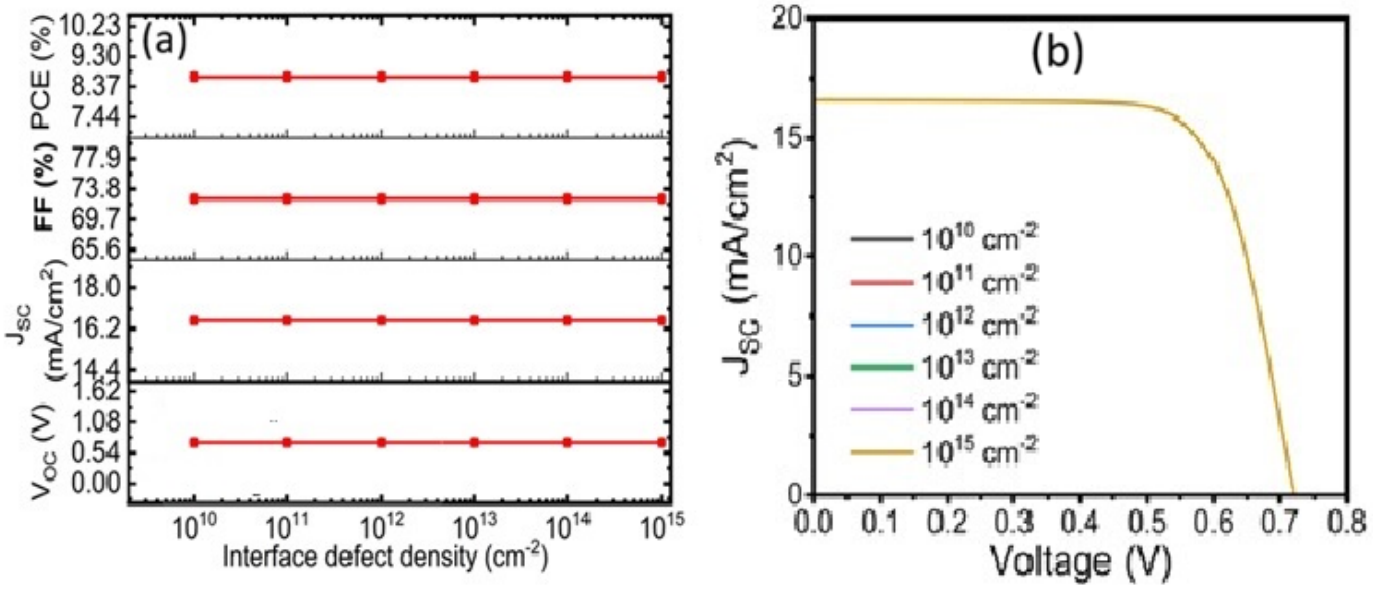

Figure 9: (a) Dependence of V_{OC}, J_{SC}, FF, and PCE on defect density of the CeO_x/absorber interface, (b) Associated J-V curves.

respectively. The stability of the photovoltaic response suggests that recombination effects at the front interface were negligible. This can be attributed to the favorable conduction band alignment between CeO_x and Cs_2TiBr_6, which supported fast electron extraction and blocking of holes from reaching the interface, to reduce the interaction of photogenerated carriers with potential recombination centers. In addition, the trap energy levels were positioned away from mid-gap, resulting in low recombination effects even at high defect density. These conditions ensured minimal impact on quasi-Fermi level splitting and helped maintain both V_{OC} and FF.

The invariance of J_{SC} further confirmed that optical absorption and charge-collection efficiency in the Cs_2TiBr_6 absorber layer were unaffected by the interface trap density. The CeO_x ETL was highly transparent due to its wide bandgap, and carrier (electron) generation and transport remained unaffected to ensure steady photocurrent. Hence the device architecture exhibited strong tolerance to CeO_x/Cs_2TiBr_6 interfacial trap density up to 10^{15} cm^{-2}. This supports the effectiveness of CeO_x as a good ETL in suppressing recombination losses at the front contact.

3.9. Influence of defect density of the absorber/Cu_2O and Cu_2O/CuO interfaces

The contour plots in Figure 10 illustrates the influence of interface defect densities (10^{10}–10^{13} cm^{-2}) at the Cs_2TiBr_6/Cu_2O and Cu_2O/CuO interfaces on the photovoltaic performance. The V_{OC} exhibited a remarkable dependence on the interface defect density at the absorber/Cu_2O interface. The Voc decreased significantly from 1.06 V to 0.72 V with increasing defect. The contour plot (Figure 10a) reflects this substantial degradation by showing a steep gradient along the Cs_2TiBr_6/Cu_2O interface axis, while negligible variation could be seen along the Cu_2O/CuO interface. This behavior could be ascribed to enhanced Shockley-Read-Hall (SRH) recombination at the Cs_2TiBr_6/Cu_2O interface, where n_1 and p_1 are the statistical carrier densities, which, along with the capture cross-section ($\sigma_{n,p}$) and total trap density (N_t), explicitly define the carrier lifetimes ($\tau_{n,p} = 1/(\sigma_{n,p} v_{th} N_t)$) displayed in Equation (9). This process reduced carrier lifetime and quasi-Fermi level splitting, leading to lower V_{OC}, FF, and PCE.

$$R_{\mathrm{SRH}}(x) = \frac{np - n_i^2}{\tau_p\,(n + n_1) + \tau_n\,(p + p_1)}, \tag{9}$$

where $R_{SRH}(x)$ is Shockley-Read-Hall recombination rate at depth x, n, and p are electron and hole concentrations, respectively, n_i is intrinsic carrier concentration of the absorber, τ_n and τ_p are electron and hole SRH lifetime (electron and hole capture lifetime), respectively. n_1 and p_1 are SRH electron and hole reference concentration, respectively. σ_n and σ_p are electron and hole capture cross section of the trap, v_{th} is thermal velocity of carriers, and N_t is bulk trap.

The minimal influence of the Cu_2O/CuO interface suggested that recombination at this interface is not a limiting factor. The J_{SC} remained constant at 16.56 mA/cm^2 across the entire range of interface traps for both interfaces (Figure 10b). This insensitivity suggested that the photogeneration and collection of carriers were not significantly hindered by interface recombination within the studied interface defect density range. The FF unveiled a slight increase from 69.83 to 72.48% with increasing Cs_2TiBr_6/Cu_2O interface defect density, as reflected in the contour plot which showed relatively weak dependence on both interfaces. In addition, the negligible impact of the Cu_2O/CuO interface further confirms that this interface does not introduce significant resistive or recombination losses. The PCE exhibited a substantial decline (12.26–8.67%) as the Cs_2TiBr_6/Cu_2O interface defect density increased.

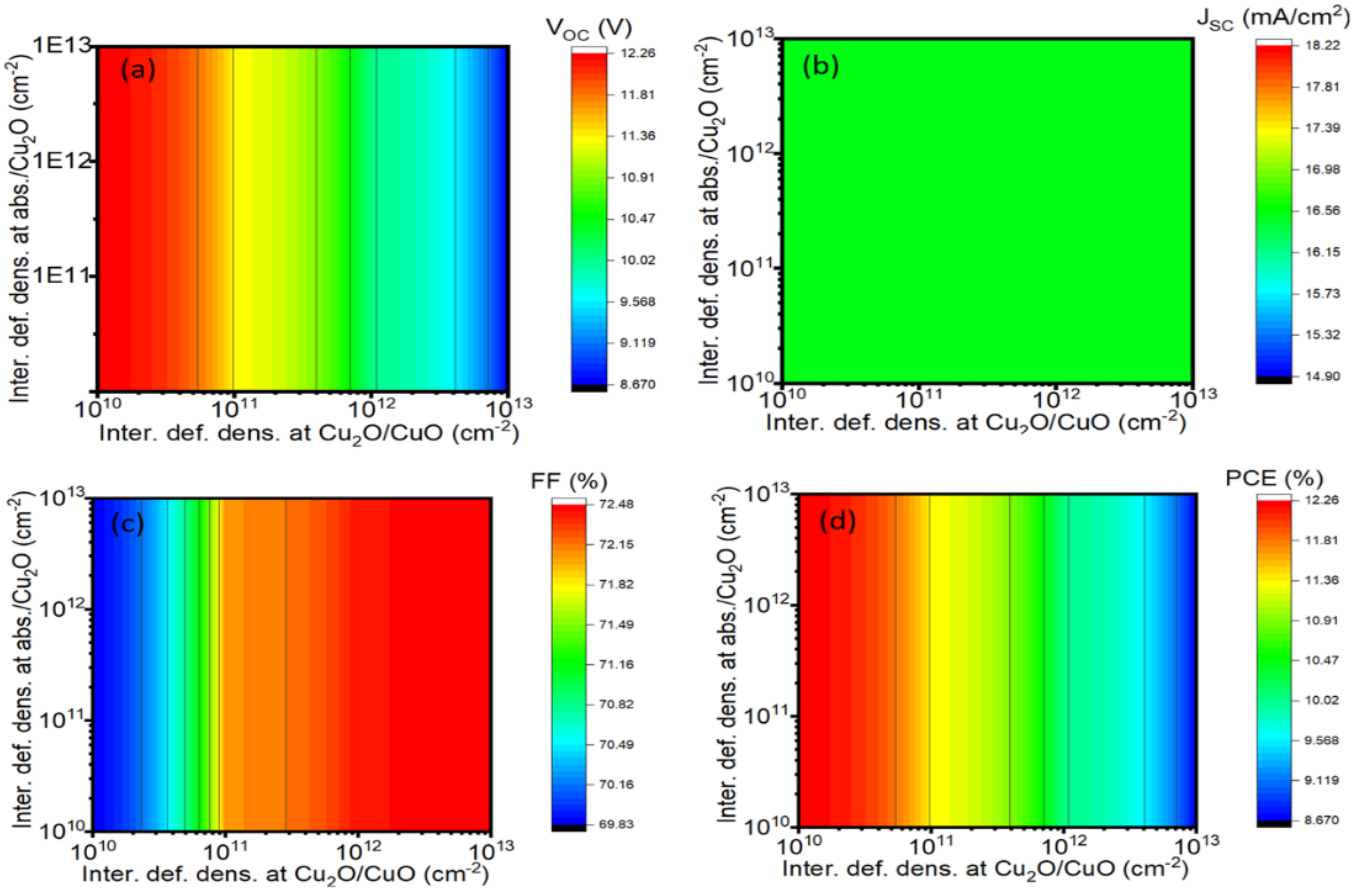

Figure 10: Contour mapping for varying (a) V_{OC}, (b) J_{SC}, (c) FF, and (d) PCE with defect densities at the absorber/Cu_2O and Cu_2O/CuO interfaces.

This trend could be seen in the contour plot, where a strong gradient is observed along the Cs_2TiBr_6/Cu_2O axis, while fixed value occurred along the Cu_2O/CuO axis.

In the Cs_2TiBr_6/Cu_2O interface, the sharp decrease in PCE could be attributed primarily to the substantial decrease in V_{OC}, because PCE is directly proportional to the product of V_{OC}, J_{SC}, and FF. Meanwhile, the constant value of PCE with varying Cu_2O/CuO defect traps could be traced to the steady values of V_{OC}, J_{SC} and FF, suggesting that these trap levels are too small to cause significant recombination of carrier.

3.10. Effect of back work function

Assessing the back-contact work function in solar cells is important because it controls energy-level alignment at the back interface, influencing carrier extraction, contact selectivity, recombination losses, and the achievable device performance [27, 30]. The role of the back metal contact was evaluated by varying the work function from 5.10 to 5.70 [14, 31]. Figure 11 revealed a significant effect of the work function on both V_{OC} and FF, while the J_{SC} remained constant at 16.57 mA/cm^2. The device exhibited a low V_{OC} of 0.72 V and FF of 72.48%, yielding a low PCE of 8.67% at the lowest work function of 5.10 eV. An increase in work function to 5.22 eV yielded a high V_{OC} of 0.77 V, an improved FF of 77.48%, resulting in a considerably higher PCE of 9.82%. Further increases in work function (≥5.50 eV) maintained this improved photovoltage but further improved FF, allowing the device to reach a maximum PCE of 9.97% at work function of 5.70 eV. This performance enhancement could be ascribed to improved energetic alignment between the metal contact and the CuO valence band. An energy barrier (non-ohmic contact) was formed at the CuO/Au interface under lower work functions [27, 31], which hindered efficient hole extraction and increased the probability of carrier accumulation and interfacial recombination [31]. An increase in work function reduced/eliminated this hole-extraction barrier, leading to improved band alignment characterized by a more ohmic hole contact. This suppressed recombination effects and reduced the series-resistance problems, leading to the improved V_{OC} and FF. The steady value of J_{SC} across all values of work function confirmed that optical absorption and photogeneration in the Cs_2TiBr_6 absorber layer were unaffected by the back-contact work function.

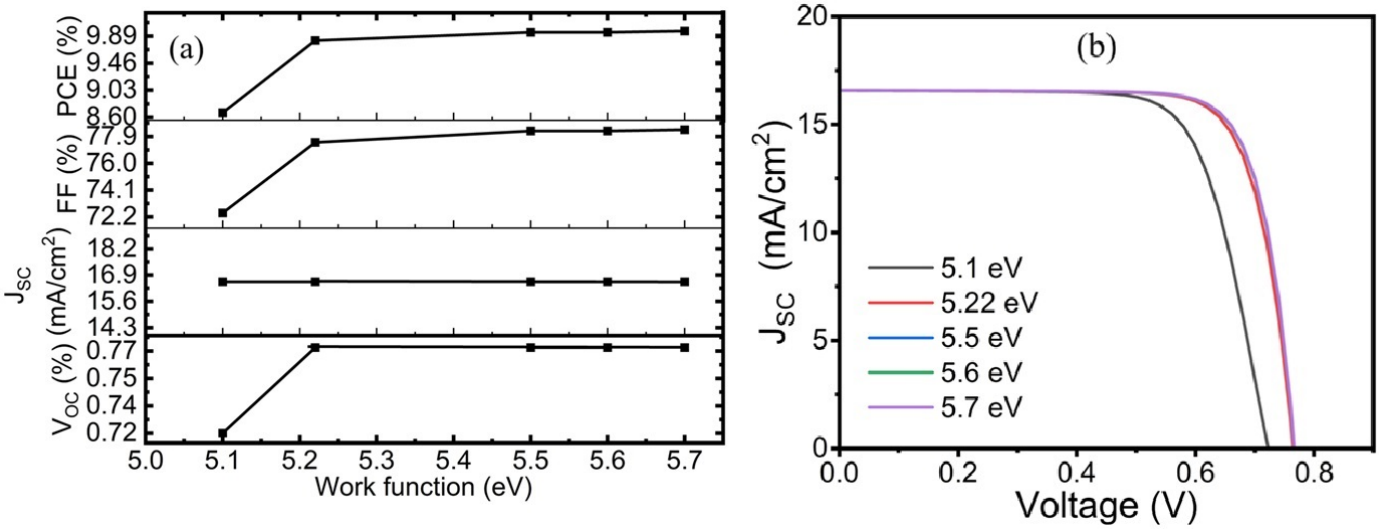

Figure 11: Variation of V_{OC}, J_{SC}, FF, and PCE with back contact work function; (b) J-V curves.

3.11. Effect of bandgap on the prototype PSC

In this work, the Cs_2TiBr_6 absorber layer was initially modeled with a bandgap of 1.8 eV in consistency with experimental literature reporting a favorable optical bandgap near 1.8 eV [32] and generally within the 1.7–1.9 eV [32] range for pure Cs_2TiBr_6. However, this bandgap is not immutable and can be narrowed experimentally through halide alloying [33, 34]. Previous studies on $Cs_2TiBr_{6-x}I_x$ have shown that partial substitution of Br by I enables significant bandgap tuning, with the optical gap narrowing across the composition series down to about 1.2 eV. Additionally, bulk mixed-halide phases such as $Cs_2TiBr_4I_2$, $Cs_2TiBr_2I_4$, and Cs_2TiI_6 have been successfully synthesized, with reported bandgap values of 1.88, 1.13, 1.04, and 1.02 eV [34]. These results confirmed that the bandgap of Cs_2TiBr_6 could be tuned from around 1.8 eV to lower values, which supports the possibility of varying the absorber optical bandgap in the range of 1.8 to 1.4 eV.

Figure 12 illustrated the influence of bandgap of the perovskite absorber on performance of the prototype device. The results showed that increasing the absorber's bandgap from 1.4 to 1.8 eV produced a progressive reduction in the PSC performance, mainly because the wider-bandgap absorber harvested a little portion of the solar spectrum, as shown in Figure 12c. As the bandgap was increased, fewer low-energy photons had sufficient energy to excite electrons from the valence band to the conduction band [35], therefore the numbers of photogenerated carriers declined. This explained the substantial reduction in the magnitude of J_{SC} (29.09–16.56 mA/cm^2). The discreet QE curves in Figure 12c illustrated a decrease in the spectrum coverage with broadening bandgap, suggesting a decline in photon absorption and carrier generation, which directly minimized the J_{SC} values.

The V_{OC} experienced a slight dip from 0.78 to 0.72 V as the bandgap increased. In the case of ideal solar cells, a larger bandgap typically supports a higher V_{OC} [35, 36] since the maximum photovoltage achievable is tied to the energy gap of the absorber [Equation (10)] [35, 36]. The open-circuit voltage (V_{OC}) is not determined only by the bandgap; it is also determined by recombination kinetics, interface defects, and energy level alignments. In this work, the simulated trend suggested that blue-shifting the absorber bandgap reduced carrier generation enough to weaken the quasi-Fermi-level separation, therefore V_{OC} did not increase and instead dropped slightly.

This suggests that the benefits expected from a larger bandgap were offset by the challenges of lower photogeneration and the related issues of transport and recombination.

$$V_{OC} = \frac{E_g}{q} - \Delta V, \tag{10}$$

where q is charge, E_g is bandgap and V is voltage loss.

The FF improved gradually from 68.36 to 72.48% with increasing bandgap. This could be explained by the lower photocurrent and reduced carrier accumulation inside the PSC, which minimized the recombination and internal resistive losses during operation. With fewer generated carriers, the device could exhibit a more ideal J-V shape, resulting in a modest improvement in FF. The PCE decreased significantly from 15.56 to 8.67%, due to the combined reduction in V_{OC}, J_{SC} and FF. These results suggest that a smaller absorber bandgap is more favorable for this perovskite, because it broadened light absorption, increased carrier generation, and improved the entire photovoltaic performance.

3.12. Impact of electron capture cross section in the absorber

The assessment of the electron capture cross section in the absorber is important because it plays a key role in determining the strength of defect-assisted recombination, thereby influencing carrier lifetime and the device performance. Experimentally,

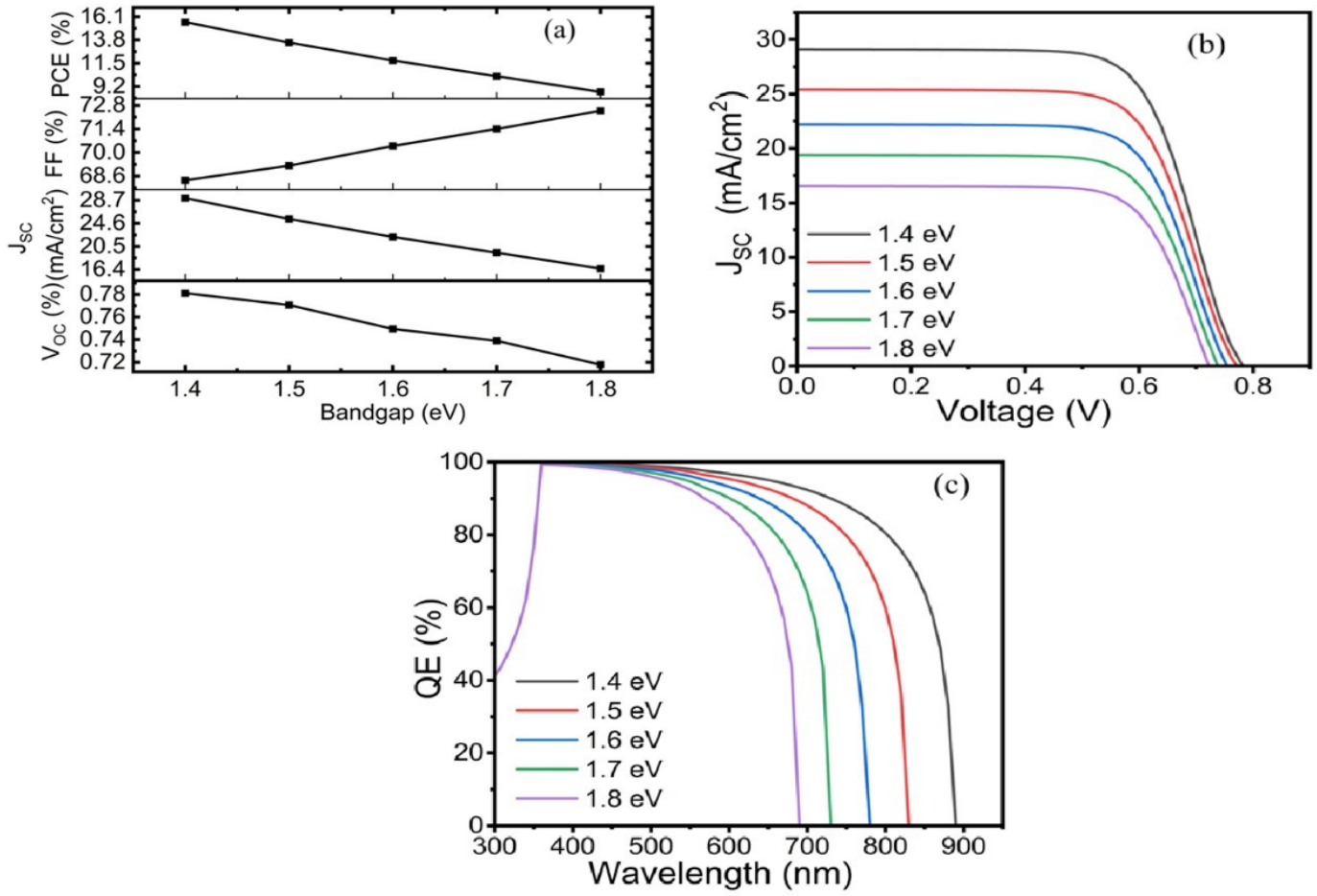

Figure 12: (a) Dependence of V_{OC}, J_{SC}, FF, and PCE with bandgap of the absorber, (b) Associated J-V curves, (c) QE plots for the PSC.

the effective electron capture cross section can be minimized by defect passivation, control of composition, improvement of film crystallization, and surface/interface engineering, which minimizes deep trap activity and reduces recombination losses. Figure 13 shows that electron capture cross-section in the absorber, increasing from 10^{-19} cm^2 to 10^{-15} cm^2, which minimizes performance. The V_{OC} remained constant at 0.72 V, J_{SC} was essentially unchanged (16.56–16.57 mA/cm^2), while FF increased slightly (72.48–73.00%), resulting in a marginal rise in PCE (8.67–8.76%).

The electron capture cross section plays a crucial role in determining how well defect states can snag free electrons during the SRH recombination process. When the capture cross section is larger, it typically boosts the chances of carriers getting trapped at defect sites, which usually leads to increased recombination losses. Interestingly, the photovoltaic parameters in this case do not show any significant decrease across the investigated range. This suggested that the device's performance was not primarily hindered by electron capture at the absorber defect states.

The invariance of V_{OC} suggested that the quasi-Fermi level splitting was not significantly altered by changing the electron capture cross section. Likewise, the fixed J_{SC} indicated that photogeneration and carrier collection remained practically unaffected, as reflected on the overlapping QE curves (Figure 13c). The small increase in FF implied a slight reduction in recombination-related carrier loss during extraction, resulting in modest improvement in PCE. This showed that the absorber electron capture cross section is a weakly sensitive parameter for this device. Nevertheless, the lower capture cross section value of 10^{-19} cm^2 is taken as the optimal for the optimized device due to 0.09% increase in PCE recorded for this cross-section value.

The overlapping QE plots (Figure 13c) shows that the photon absorption and carrier generation did not change with increasing electron capture cross section. This supports the constant value of J_{SC} recorded in this investigation (Figure 13b).

3.13. Optimized device

A few optimal simulation parameters were obtained from the prototype device simulations to substitute into the SCAPS-1D software to simulate the Cu_2O/CuO double HTL-assisted device in order to achieve improved performance. The few optimal input

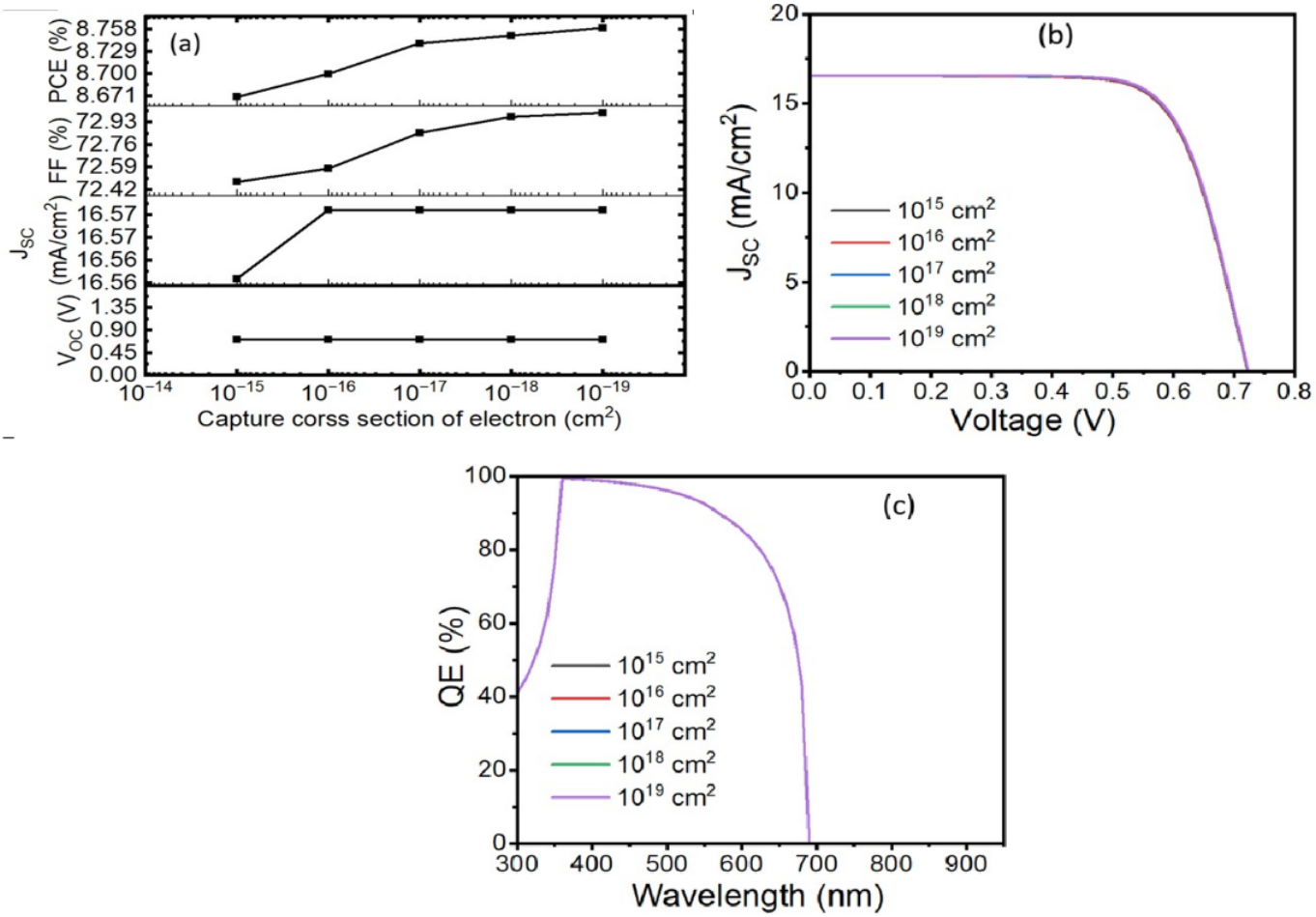

Figure 13: (a) Dependence of V_{OC}, J_{SC}, FF, and PCE on electron capture cross section in the absorber, (b) J-V curves, (c) QE plots.

values include the increased optimal thicknesses of 1.4 μm, 1.0 μm, and reduced thickness of 0.1 μm for the absorber, Cu_2O and CuO, respectively. Defect densities of CeO_x ETL and Cu_2O HTL were reduced to 1×10^{15} cm^{-3}, while of the CuO was raised to 1×10^{14} cm^{-3} according to the minimum value of bulk defect trap that can be achieved experimentally. Acceptor carrier concentration of Cu_2O HTL was raised to 1×10^{18} cm^{-3} to increase conductivity of the HTL and to improve hole transport. The optimal back contact work function is 5.7 eV for Pt. All interface defect density were reduced to 1×10^{10} cm^{-2}, according to experimental standard [19, 21, 37]. The thickness of the ETL and all other parameters remained the same as in the case of the prototype device simulation.

The optimized device (Figure 14) achieved an improved PCE of 30.75%, a significantly increased V_{OC} (1.15 V), J_{SC} (32.14 mA/cm^2), and FF (82.85%). The substantial increase in V_{OC} compared to the prototype device (0.72 V) reflect a substantial reduction in non-radiative recombination losses within both the absorber and the back charge-selective interface. The higher carrier concentration (doping level) in the Cu_2O HTL helped to lower its resistivity for improved hole mobility and conductivity. This strengthened the built-in electric field at the Cs_2TiBr_6/Cu_2O interface, facilitated faster hole extraction and reduced carrier accumulation and recombination losses at the interface, leading to an improved V_{OC}. Lower absorber bulk defect density extended carrier lifetime and maintained a larger quasi-Fermi level splitting under illumination, while reduced interfacial traps at the Cs_2TiBr_6/Cu_2O interface suppressed recombination at the hole extraction interface to boost the device performance.

The substantial improvement in J_{SC} (Figure 14a) come from enhanced photon harvesting enabled by the increased absorber thickness, which allowed deeper penetration and more complete utilization of the solar spectrum. This could be supported by the increase in QE up to 100% in the wavelength region (400–800 nm) of the solar spectrum (Figure 14b), indicating improved carrier generation. Reducing the optical bandgap of the absorber from 1.8 to 1.4 eV extends the absorption edge from ~690 nm to ~890 nm to enable efficient harvesting of additional photons in the red and near-infrared region. This resulted in an enhanced and broader QE response up to 100% over a wider spectral range, which significantly increased the J_{SC} to 32.14 mA/cm^2.

The enhancement in the transport of carrier could be ascribed to the high mobility Cu_2O HTL, which allowed for efficient hole extraction without adding resistive losses. Furthermore, the thinner CuO HTL assisted to reduce unwarranted light absorption and reduced the series resistance from the back contact area. The substantial enhancement in FF could be traced to better charge extraction

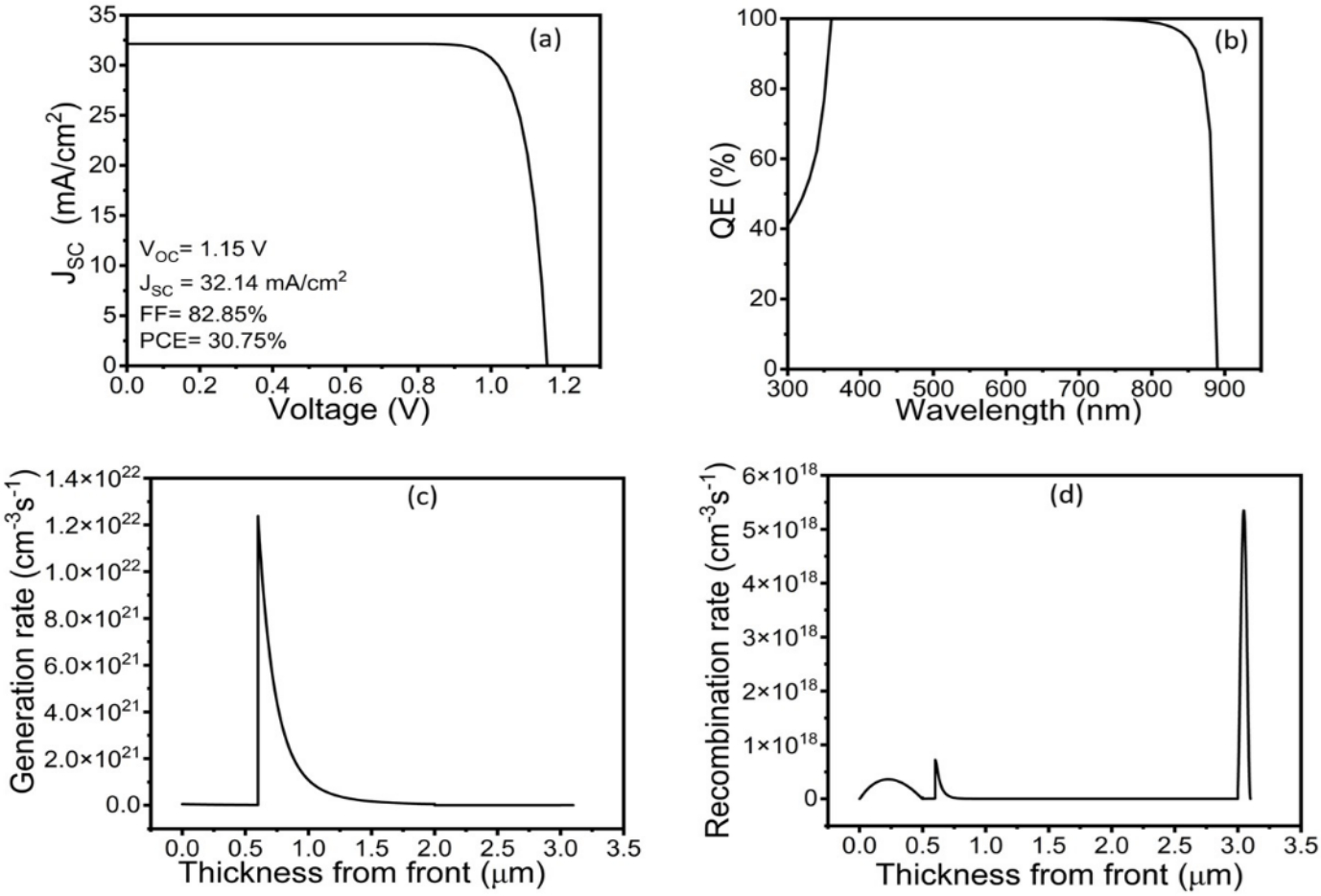

Figure 14: Optimized Cu_2O/CuO double HTL-free PSC.

and contact energetics. With a high work function value of 5.7 eV, platinum effectively removed the barrier for hole extraction at the CuO interface, leading to an Ohmic contact with the hole barrier height less than zero, that minimized charged accumulation and resistive voltage drops. These improvements synergized to reduce recombination effects, improved the distribution of the built-in electric field, and ensured efficient charge extraction, leading to a well-rounded enhancement across all PV parameters. It is worth mentioning that the PCE value of 30.75% agrees with the Shockley-Queisser efficiency limit of 32.91% for single junction solar cells that employ an absorber with a bandgap of 1.4 eV [38]. This supports the PCE observed in the current PSC.

Figure 14c demonstrates the carrier generation rate, which exhibits its peak within the perovskite absorber region, with peak values in the order of 1.24 $\times 10^{22}$ cm^{-3}s^{-1} near the front interface (CeO_x/Cs_2TiBr_6). This high generation rate could be attributed to effective photon absorption. This is followed by a gradual decay toward the back contact due to attenuation of the incident photon flux. The carrier generation profile remains substantial across the entire absorber thickness of 1.4 μm, indicating strong light harvesting throughout the bulk, which is consistent with the high J_{SC} (32 mA/cm^2) obtained from the optimized device. In contrast, the recombination rate (Figure 14d) is remarkably lower than the generation rate, indicating efficient charge extraction. The recombination rate is relatively minimal in the absorber with value of 3.69 $\times 10^{15}$ cm^{-3}s^{-1} due to the moderate bulk defect density of 10^{14} cm^{-3}. Higher recombination rates were observed near the interfaces, particularly at the CeO_x/Cs_2TiBr_6 (7.54 $\times 10^{17}$ cm^{-3}s^{-1}) and Cs_2TiBr_6/Cu_2O (5.37 $\times 10^{18}$ cm^{-3}s^{-1}). However, these values remained relatively low due to the optimized interface defect density of 10^{10} cm^{-2}, which effectively suppressed trap-assisted recombination.

3.13.1. Influence of operating temperature on the optimized cell

Temperature-dependent analysis is essential for solar cells due to the sensitivity of perovskite compositions to temperature because of the presence of organic cations [2, 39, 40]. The temperature dependence of the optimized FTO/CeO_x/Cs_2TiBr_6/Cu_2O/CuO/Pt solar cell was evaluated over the range of 290–400 K to assess its operational confidence under practical environmental conditions. The device exhibited a gradual deterioration in performance with elevating temperature (Figure 15), which is consistent with the well-established thermally activated recombination behaviour in semiconductor junctions [18, 41].

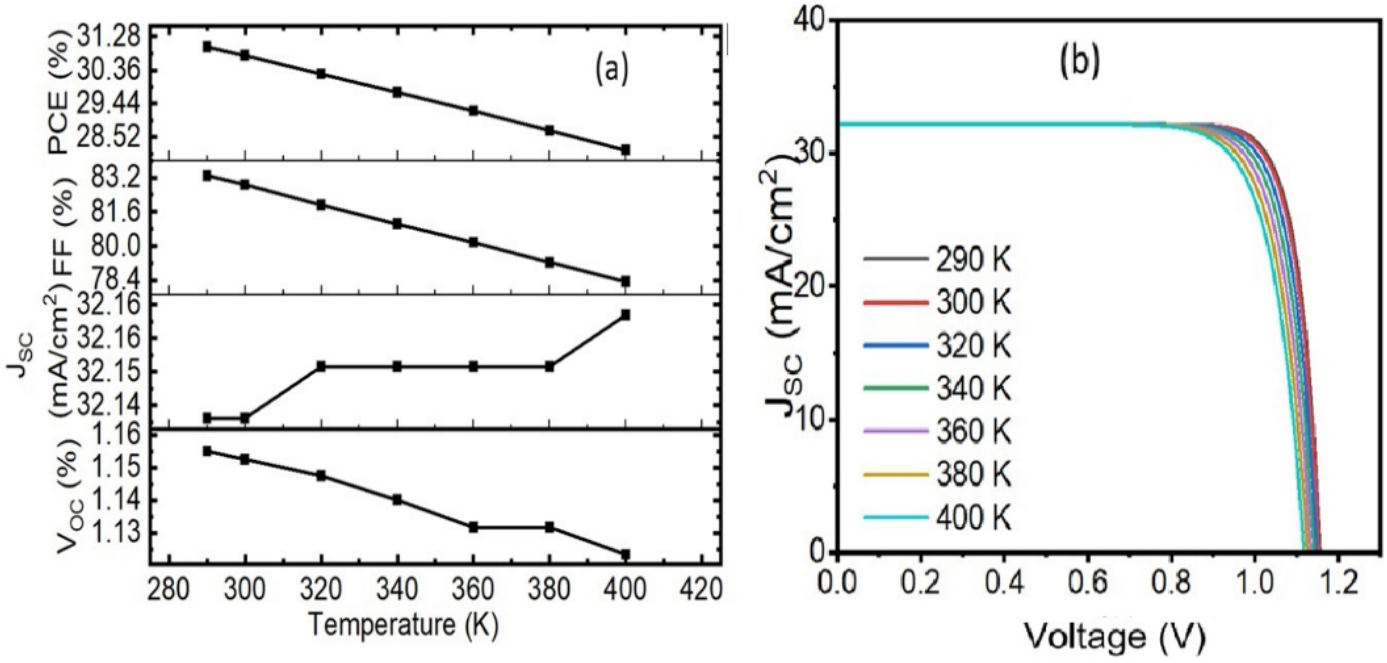

Figure 15: (a) Variation of V_{OC}, J_{SC}, FF, and PCE with operating temperature of the Cu_2O/CuO HTL-free PSC, (b) Associated J-V curves.

The PSC demonstrates a gradual degradation in performance with increasing temperature. The most noticeable effect was the drop in V_{OC}, which declined from 1.16 V at 290–300 K down to 1.12 V at 400 K. This decline in V_{OC} is a common effect in solar cells when temperatures rise, mainly because of increased thermally activated carrier recombination and a decrease in quasi-Fermi level splitting [41]. In another way, J_{SC} remained unchanged only increasing slightly from 32.14 mA/cm^2 at 290–300 K to 32.16 mA/cm^2 at the temperature peak of 400 K. This showed that temperature did not significantly affect photon absorption and carrier generation in the device and the J_{SC} stayed relatively stable throughout the investigated temperature range. The FF decreased steadily with temperature, declining from 83.29 to 78.33% at 400 K. This dip suggests worsening carrier transport and Increased resistive and recombination losses at higher temperatures [41]. The combined result of the reduction in V_{OC} and FF, led to a significant drop in the PCE (30.99–28.16%), corresponding to a total loss of 2.83% points. Nevertheless, the device exhibits good thermal stability since the PCE remained above 28% even at 400 K, but its best performance could be achieved at lower temperature.

3.14. Simplification of the optimized PSC architecture

Simple PSC architectures are desired because of their reduced complexity due to the fewer stacked layers, and expected lower production costs [42]. In addition, it minimizes interfacial defects, thereby minimizing recombination losses and improving charge transport. Fewer layers also boost device stability by eliminating unstable materials. This simplification ensures better reproducibility and scalability for large-area fabrication. Such simple designs have been demonstrated to maintain high efficiency while improving durability [43]. Therefore, this section investigates the FTO/CeO_x/Cs_2TiBr_6/Cu_2O/Pt single HTL-free (or Cu_2O-assisted) (Figure 16a) and FTO/CeO_x/Cs_2TiBr_6/Pt HTL-free (Figure 16b) simpler architectures.

The band diagram of the simple Cu_2O single HTL-assisted PSC showed a well-aligned selective-contact structure across the device (Figure 17a). A very small conduction-band offset of about 0.07 eV is formed at the CeO_x/Cs_2TiBr_6 interface, which is favorable for electron extraction. At the back side, the Cu_2O with an electron affinity 3.5 eV and bandgap of 2.2 eV give a valence-band position that is close enough to that of Cs_2TiBr_6 to permit hole transfer, while still providing a sturdy barrier against electrons. The increased absorber thickness and reduced interface defect enhanced the band bending and reduced recombination in the device. The quasi-Fermi-level splitting is wide, which is consistent with the observed comparable value of V_{OC} (1.15 V). Meanwhile, the optimized HTL-free cell does not contain any HTL (Figure 17b). Herein, the front contact alignment remained favorable because the CeO_x/Cs_2TiBr_6 conduction-band offset remained unchanged (0.07 eV), supporting efficient electron extraction. However, the absorber contacts the metal directly at the back side, which makes the back contact to become less selective. This resulted to an increase in recombination at the rear interface. This could be seen in the smaller quasi-Fermi-level splitting in (Figure 17b). Although the device still shows strong carrier collection potential, but a substantial drop in V_{OC} is expected.

Figure 17c demonstrated the photovoltaic performance of the Cu_2O HTL-assisted and HTL-free simple PSC designs. The optimized Cu_2O HTL-assisted cell gave nearly identical values of V_{OC}, J_{SC}, FF and PCE as 1.15 V, 32.14 mA/cm^2, 82.87%,

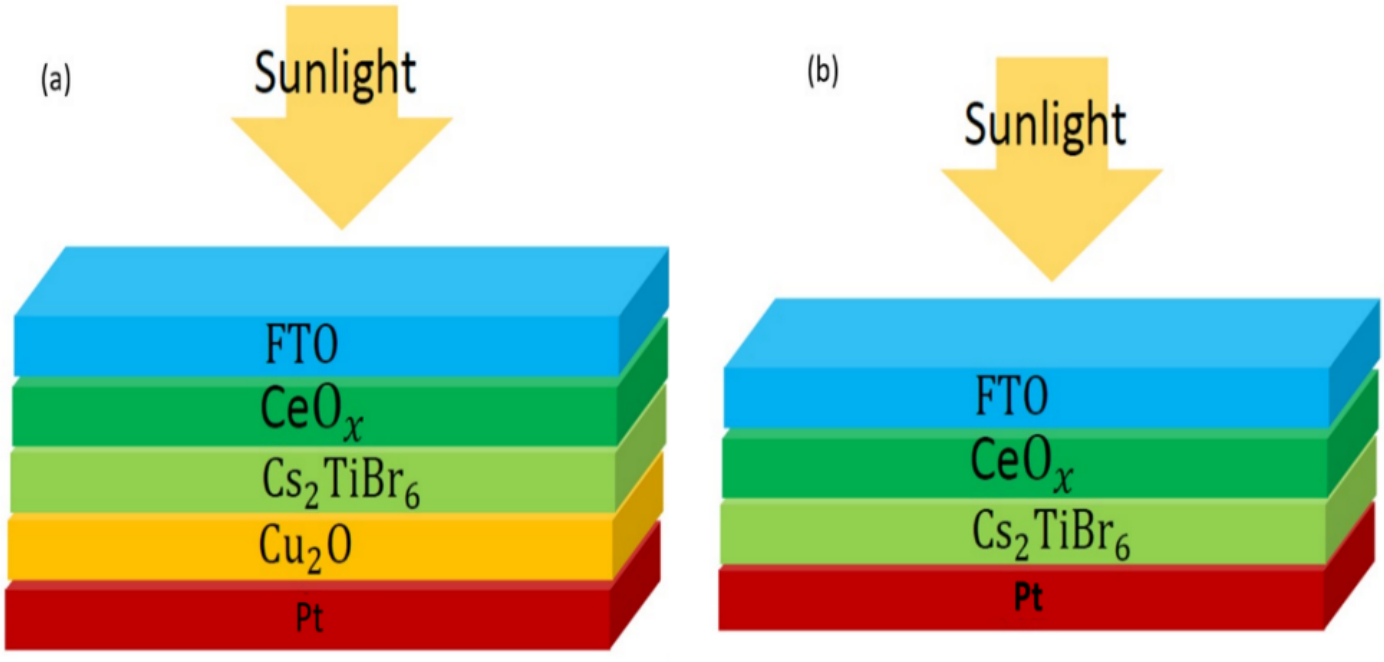

Figure 16: Schematic illustration of (a) Cu_2O HTL-assisted, and (b) HTL-free PSC architectures.

and 30.76%, respectively. This shows that removing CuO HTL after optimization does not degrade performance. It could be seen that the difference in PCE is only 0.01%, and the FF difference is only 0.02%. That means Cu_2O alone is sufficient as the HTL (to sufficiently extract holes) provided the defect densities and thicknesses are optimized. Compared with the prototype ($FTO/CeO_x/Cs_2TiBr_6/Cu_2O/CuO/Au$) device (Figure 3 and Table 3), the optimized Cu_2O HTL-assisted device showed a gain of 0.43 V in V_{OC}, an increase of 15.57 mA/cm^2 in J_{SC}, about 10.39% boost in FF, and an increase in PCE of 22.09% points. For the HTL-free architecture, the J_{SC} is also almost the same as the Cu_2O HTL-free PSC, since 32.11 mA/cm^2 is only lower by a magnitude of 0.03 mA/cm^2, but the PCE is reduced by 8.44% points because the V_{OC} declined from 1.15 to 0.82 V. The lower performance of the HTL-free PSC could be attributed to the absence of a hole-selective layer, which increased back-contact recombination and lowered quasi-Fermi level splitting, resulting in a significant drop in V_{OC} and PCE despite comparable J_{SC}.

Figure 17d demonstrated that both optimized cells have very high QE over a broad spectral range. The QE is 100% through most of the visible region (400–800 nm), indicating highly efficient photocarrier generation and collection. The overlapping QE curves for both devices explained why their J_{SC} values are nearly identical (32.14 mA/cm^2 for the Cu_2O HTL-assisted cell and 32.11 mA/cm^2 for the HTL-free PSC). Thus, the lower PCE of the HTL-free cell is not due to weaker light absorption, but due mainly to its smaller V_{OC} value caused by stronger back-contact recombination.

Figure 18 illustrated carrier generation and recombination rates for the Cu_2O HTL-free and HTL-free PSCs. Both devices exhibited similar generation profiles, with peak values of 1.23×10^{22} cm^{-3}s^{-1} near/at 0.6 μm, followed by a rapid decay toward the back of the cell. The nearly identical generation rates support the comparable J_{SC} (~32 mA/cm^2) in both PSCs. The Cu_2O HTL-assisted cell showed a localized recombination peak of 7.39×10^{17} cm^{-3}s^{-1} near/at the front of the absorber, with negligible recombination elsewhere. In contrast, the HTL-free design exhibited slightly lower recombination rate of 6.55×10^{17} cm^{-3}s^{-1}. It should be noted that the HTL-free cell showed slightly reduced recombination around 0.6 μm due to the absence of the Cs_2TiBr_6/Cu_2O interface. However, the lack of a hole-selective layer resulted in increased back-contact recombination and reduced quasi-Fermi level splitting, which lowered the device performance.

Table 5 reveals that these optimized devices ($FTO/CeO_x/Cs_2TiBr_6/Cu_2O/CuO/Pt$, $FTO/CeO_x/Cs_2TiBr_6/Cu_2O/Pt$ and $FTO/CeO_x/Cs_2TiBr_6/Pt$) performed appreciably, when compared with the Cs_2TiBr_6-based PSCs in the literature. It could be seen that the highest PCE recorded for this absorber is 26.96%. The lower performances reported by the published works could be attributed primarily to the higher bandgaps of 1.7 and 1.8 eV employed in the simulations [4, 9–11, 44]. Meanwhile, the superior higher PCEs of 30.75 and 30.76% recorded by the current simulations could be traced primarily to the lower bandgap of 1.4 eV which extend the absorption edge of the Cs_2TiBr_6 to improve photon absorption range and carrier generation. This shows that bandgap is one of the major optoelectronic parameters that limit the performance of absorbers. Interestingly, the HTL-free design also recorded a PCE (22.32%) that compete with most of the published values, further confirming that bandgap narrowing of the absorber is an essential strategy to improve the photovoltaic performance of PSCs utilizing this absorber. The HTL-free architecture marks the first investigation of this simple architecture for the Cs_2TiBr_6-based PSCs.

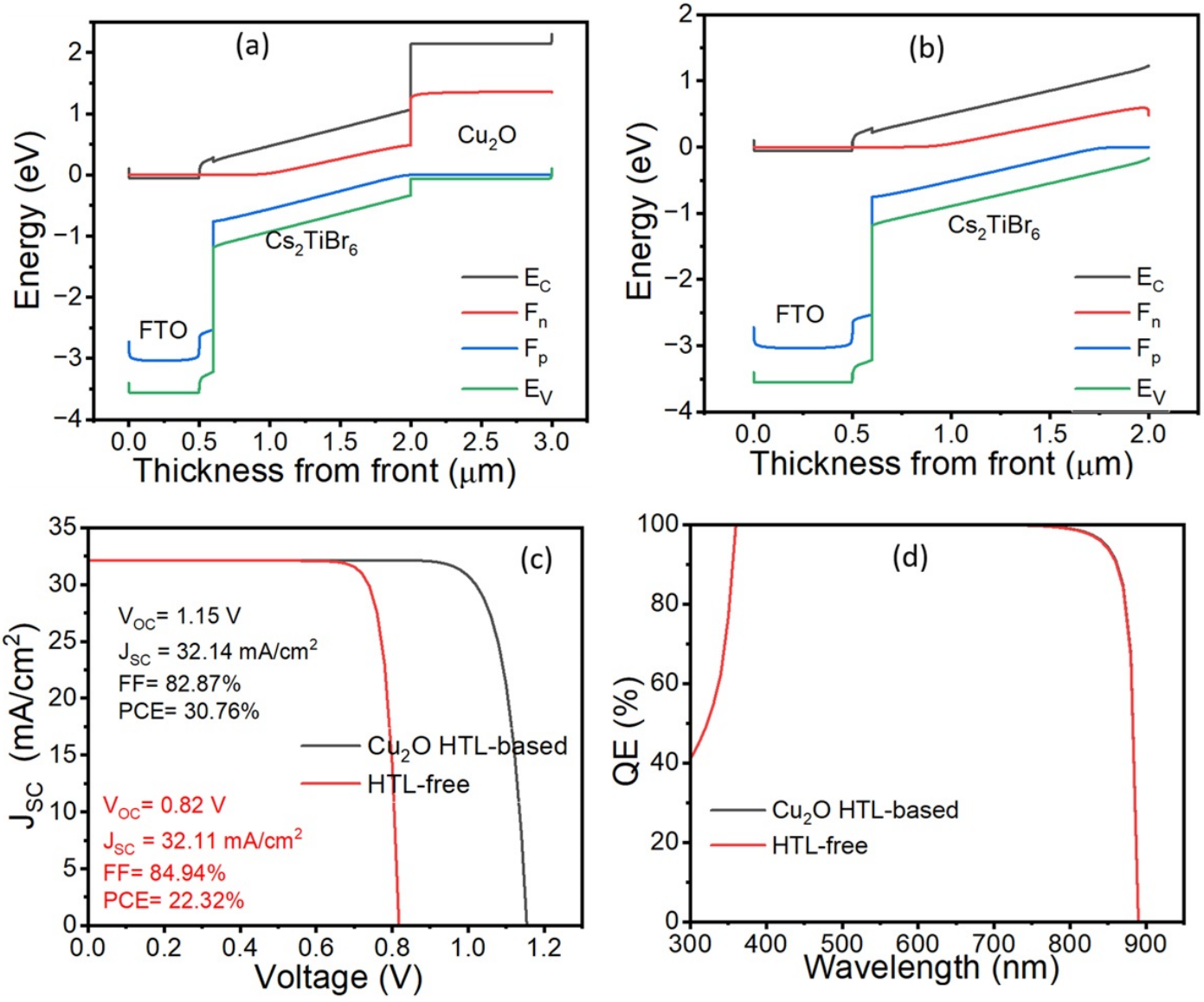

Figure 17: (a) Energy band plots of the optimized Cu_2O HTL-free cell, (b) Energy band plots of the optimized HTL-free PSC, (c) J-V curves for the Cu_2O HTL-free and HTL-free cells, (d) QE plots of the Cu_2O HTL-free and HTL-free.

Table 5: Overview of performance metrics for Cs_2TiBr_6-based PSCs.

Perovskite solar cell	Nature of hole transport	Preparation method	V_{OC} (V), J_{SC} (mA/cm^2), FF (%), PCE (%)	Reference
FTO/CeO_x/Cs_2TiBr_6/Cu_2O/CuO/Pt	HTL-free	SCAPS-1D	1.15, 32.14, 82.85, 30.75	This work
FTO/CeO_x/Cs_2TiBr_6/Cu_2O/Pt	HTL-free	SCAPS-1D	1.15, 32.14, 82.87, 30.76	This work
FTO/CeO_x/Cs_2TiBr_6/Pt	HTL-free	SCAPS-1D	0.82, 32.11, 84.94, 22.32	This work
FTO/TiO_2/Cs_2TiBr_6/Au	HTL-free	Experiment	0.89, 2.34, NA, NA	[6]
FTO/TiO_2/Co_{60}/Cs_2TiBr_6/P_3HT/Au	HTL-free	Experiment	1.02, 5.69, 56.4, 3.28	[8]
FTO/TiO_2/Cs_2TiBr_6/$CuSbS_2$/P_3HT/Au	HTL-free	SCAPS-1D	1.02, 26.20, 79.9, 21.30	[45]
FTO/ZnO/Cs_2TiBr_6/$CuSbS_2$/Pt	HTL-free	SCAPS-1D	1.05, 31.63, 81.36, 26.96	[9]
ITO/LBSO/Cs_2TiBr_6/CNTS/Au	HTL-free	SCAPS-1D	1.12, 26.63, 82.94, 24.82	[4]
FTO/SnO_2/Cs_2TiBr_6/CBTS/Au	HTL-free	SCAPS-1D	1.31, 20.76, 88.9, 24.24	[10]
FTO/CdS/Cs_2TiBr_6/Cu_2SbS_2/Au	HTL-free	SCAPS-1D	1.15, 24.39, 84.76, 23.77	[11]

3.14.1. Physical significance of dual HTL in the presence of comparable single HTL efficiency

Although the optimized Cu_2O/CuO dual HTL-assisted and Cu_2O single HTL-free devices exhibited identical PCE values, the dual HTL architecture played a critical role in establishing favorable band alignment and improved carrier selectivity. The CuO layer

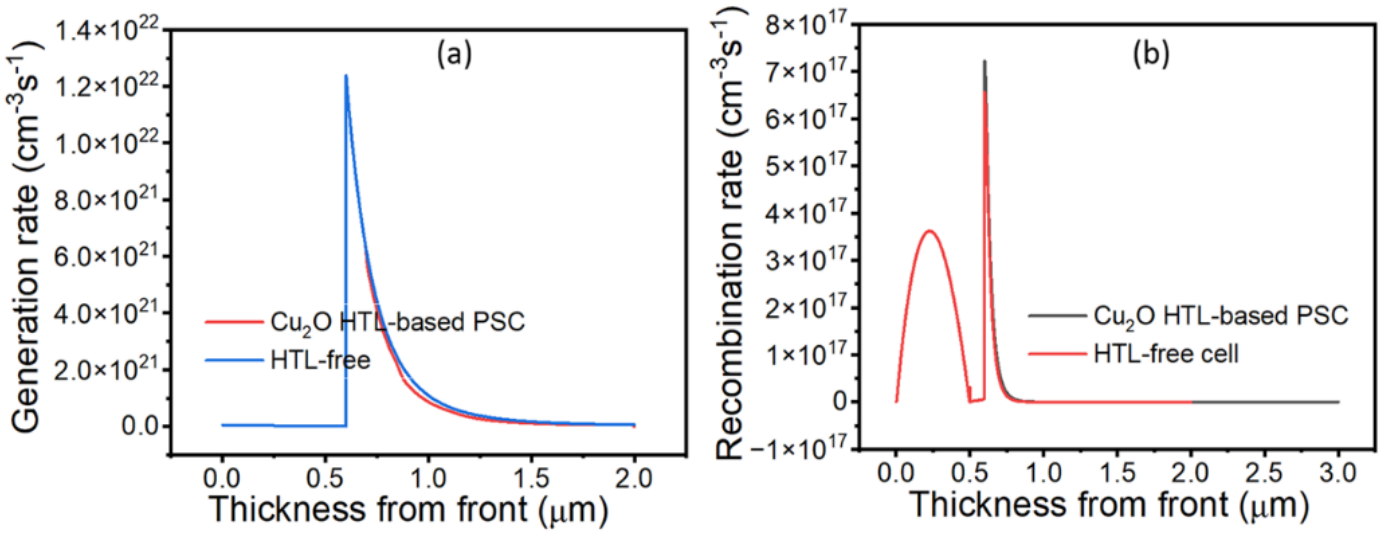

Figure 18: (a) Carrier generation rates for the Cu_2O HTL-free and HTL-free cells, (b) Carrier recombination rates for the Cu_2O HTL-free and HTL-free cells.

introduced a graded energy-level transition that improved hole extraction and suppressed back-electron injection, thereby reducing interfacial recombination. Nevertheless, under optimized conditions where thicknesses and defect densities are carefully controlled, the Cu_2O layer alone became sufficiently efficient to facilitate near-ideal charge extraction, resulting in comparable device output.

This finding suggests that although dual-HTL engineering can improve interfacial energetics and carrier selectivity, the additional interface introduced by the Cu_2O/CuO bilayer does not necessarily guarantee superior photovoltaic performance when compared with the properly optimized single-HTL structure. Therefore, the simpler Cu_2O-only configuration may offer a more practical balance between efficiency, fabrication simplicity, and reduced interfacial recombination. Additionally, the dual HTL structure may still remain beneficial for improving device robustness and interfacial quality under non-ideal fabrication conditions or experimentally imperfect interfaces [46].

4. Conclusion

This study employed the SCAPS-1D numerical simulation program to design and optimize high-performance lead-free Cs_2TiBr_6-based PSCs using CeO_x as the ETL and Cu_2O/CuO as dual HTLs. The photovoltaic performance of the proposed structures was systematically investigated by varying critical device parameters, including layer thickness, absorber bandgap, carrier concentration, defect density, interface defect density, electron capture cross-section, and back-contact work function. In addition to the dual-HTL structure, simplified single-HTL and HTL-free device configurations were also evaluated to explore the likelihood of reducing fabrication complexity and production cost. The optimized FTO/CeO_x/Cs_2TiBr_6/Cu_2O/CuO/Pt cell achieved a remarkable PCE of 30.75%, with a V_{OC} of 1.15 V, J_{SC} of 32.14 mA/cm^2, and FF of 82.85%. The significant enhancement in photovoltaic performance was ascribed to improved interfacial band alignment, efficient carrier extraction, reduced recombination losses, broadened optical absorption, and improved built-in electric field distribution across the device interfaces. The optimized single-HTL Cu_2O-based device (FTO/CeO_x/Cs_2TiBr_6/Cu_2O/Pt) recorded a comparable PCE of 30.76%, demonstrating that Cu_2O alone can effectively facilitate hole carrier extraction after proper optimization. Meanwhile, the HTL-free structure (FTO/CeO_x/Cs_2TiBr_6/Pt) achieved a competitive PCE value of 22.32%, indicating the feasibility of simpler and lower-cost device architectures. Furthermore, the optimized dual-HTL device demonstrated good thermal stability by maintaining a PCE above ~28% within the temperature range of 290–400 K. Comparative analysis with previously reported Cs_2TiBr_6-based PSCs showed that the proposed configurations outperform many existing theoretical and experimental designs. The results of this study demonstrate that appropriate interface engineering, defect minimization, charge transport layer optimization, and bandgap tuning are effective strategies for enhancing the performance of lead-free PSCs. The high PCEs obtained using environmentally friendly Cs_2TiBr_6 highlight the significant potential of lead-free PSCs for future sustainable photovoltaic applications. Although the present work is based on numerical simulations, the findings provide valuable theoretical guidance for future experimental development of efficient, stable, scalable, and cost-effective PSCs. Although experimentally fabricated devices were not developed in the present study, the simulation framework and optimization parameters were carefully restrained using experimentally reported material properties and realistic interface conditions, consequently improving the practical relevance of the obtained findings.

Data availability

Data will be made available upon reasonable request to the corresponding author.

Declaration of competing interest

The authors declare that they have no known competing financial interests or personal relationships that could have appeared to influence the work reported in this manuscript.

Funding

This work was supported by the UKRI Ayrton Fund through the REACH-PSM project: Resilient Renewable Energy Access through Community-Driven Holistic Development in Perovskite Solar Module Manufacturing.

References

[1] F. Zhou, Y. Zhang, J. Wu, W. Yang, X. Fang, T. Jia, Y. Ling, P. He, Q. Liu & J. Lin, "Utilizing Er-doped $ZnIn_2S_4$ for efficient photocatalytic CO_2 conversion", Applied catalysis B **341** (2024) 123347. https://doi.org/10.1016/j.apcatb.2023.123347.

[2] P. R. Jubu, Z. S. Mbalaha, E. V. Tikyaa, O. S. Obaseki, K. O. Ighodalo, O. Adedokun, A. Nathan-Abutu, M. B. Ochang, Y. Yusof & M. Z. Pakhuruddin, "High-efficiency hole transport layer-free perovskite solar cells utilizing TiO_2, ZnO and bilayer TiO_2/ZnO electron transport layers: a simulation approach", Next materials **9** (2025) 101166. https://doi.org/10.1016/j.nxmate.2025.101166.

[3] W. Lin, X. Chen, Z. Ji, W. Gao, N. Zhao, M. Li, D. Zhang, Y. Ling, J. Wu, K. Huang & J. Yu, "Optimization of Cs_2TiBr_6-based perovskite solar cells with double hole transport layer by SCAPS-1D simulation", Materials today communications **46** (2025) 112841. https://doi.org/10.1016/j.mtcomm.2025.112841.

[4] M. K. Hossain, S. Islam, M. N. Sakib, M. S. Uddin, G. F. I. Toki, M. H. K. Rubel, J. Nasrin, S. H. Shahatha & M. R. Mohammad, "Exploring the optoelectronic and photovoltaic characteristics of lead-free Cs_2TiBr_6 double perovskite solar cells: a DFT and SCAPS-1D investigation", Advanced electronic materials **11** (2025) 2400348. https://doi.org/10.1002/aelm.202400348.

[5] P. R. Jubu, M. K. Omar & M. Z. Pakhuruddin, "High-efficiency p-InGaN/n-InGaN single homojunction solar cell derived by numerical simulation", Physica scripta **100** (2025) 1. https://doi.org/10.1088/1402-4896/ade74b.

[6] R. Sen & M. Yadav, "Efficient design and fabrication of Cs_2TiBr_6-based HTL-free solar cells", Journal of electronic materials **53** (2024) 1975. https://doi.org/10.1007/s11664-024-10929-w.

[7] S. Gupta, J. Kaur, R. Basu, A. K. Sharma, R. Pandey & J. Madan, "Lead-free Cs_2TiBr_6 perovskite solar cells achieving high power conversion efficiency through device simulation", Micro and nanostructures **196** (2024) 207991. https://doi.org/10.1016/j.micrna.2024.207991.

[8] M. Chen, A. D. Carl, Y. Zong, R. L. Grimm, J. Gu, X. -C. Zeng & N. P. Padture, "Cesium titanium (IV) bromide thin films based stable lead-free perovskite solar cells", Joule **2** (2018) 558. https://doi.org/10.1016/j.joule.2018.01.009.

[9] H. Karmaker, A. Siddique & B. K. Das, "Numerical investigation of lead-free Cs_2TiBr_6-based perovskite solar cell with optimal selection of electron and hole transport layer through SCAPS-1D simulation", Results in optics **13** (2023) 100571. https://doi.org/10.1016/j.rio.2023.100571.

[10] G. K. Grandhi, A. Matuhina, M. Liu, S. Annurakshita, H. Ali-Löytty, G. Bautista & P. Vivo, "Lead-free cesium titanium bromide double perovskite nanocrystals", Nanomaterials **11** (2021) 1458. https://doi.org/10.3390/nano11061458.

[11] P. A. M. Mercy & K. S. J. Wilson, "Development of environmentally friendly high-performance Cs_2TiBr_6-based perovskite solar cell using numerical simulation", Applied surface science advances **15** (2023) 100394. https://doi.org/10.1016/j.apsadv.2023.100394.

[12] E. Danladi, D. S. Dogob, S. U. Michael, F. O. Uloko & A. O. Salawu, "Recent advances in modeling of perovskite solar cells using SCAPS-1D: effect of absorber and ETM thickness", East European journal of physics **4** (2021) 5. https://doi.org/10.26565/2312-4334-2021-4-01.

[13] Z. Xing, S. -H. Li, B. -S. Wu, X. Wang, L. -Y. Wang, T. Wang, H. -R. Liu, M. -L. Zhang, D. -Q. Yun, L. -L. Deng, S. -Y. Xie, R. -B. Huang & L. -S. Zheng, "Photovoltaic performance and stability of fullerene/cerium oxide double electron transport layer superior to single one in p-i-n perovskite solar cells", Journal of power sources **389** (2018) 13. https://doi.org/10.1016/j.jpowsour.2018.03.079.

[14] E. Danladi, E. E. Oguzie & F. I. Ezema, "Highly efficient 25.562% $Cs_2AgBiBr_6$ double perovskite solar cell with copper barium tin sulfide and ZnO as charge transport channels: an intuition from a theoretical study using SCAPS-1D", Journal of photonics for energy **15** (2025) 024501. https://doi.org/10.1117/1.JPE.15.024501.

[15] C. Lin, G. Liu, X. Xi, L. Wang, Q. Wang, Q. Sun, M. Li, B. Zhu, D. P. Lara & H. Zai, "The investigation of the influence of a Cu_2O buffer layer on hole transport layers in $MAPbI_3$-based perovskite solar cells", Materials **15** (2022) 8142. https://doi.org/10.3390/ma15228142.

[16] F. Hazeghi, S. Mozaffari & S. M. B. Ghorashi, "Metal organic framework-derived core-shell CuO@NiO nanospheres as hole transport material in perovskite solar cell", Journal of solid state electrochemistry **24** (2020) 1427. https://doi.org/10.1007/s10008-020-04643-w.

[17] Q. Y. Tey, W. C. Ng & M. N. Chong, "Surface and interface engineering of p-type Cu_2O-CuO heterostructures featuring innovative 2D-CuO nanoflake morphology on Cu_2O thin film for enhanced photoelectrochemical water splitting", Applied surface science **716** (2026) 164622. https://doi.org/10.1016/j.apsusc.2025.164622.

[18] E. Danladi, L. F. Koao, T. E. Motaung & S. V. Motloung, "Defect control and performance optimization in Li^+/Na^+ co-doped HTL-free $Cs_2AgBiBr_6$ double perovskite solar cells: toward an efficient HTL-free architecture", Journal of the Indian Chemical Society **103** (2026) 102453. https://doi.org/10.1016/j.jics.2026.102453.

[19] S. Wang, Z. Dong, H. Li & J. Zhang, "Defect passivation strategies in perovskite solar cells: roles, mechanisms and progress", Journal of materials science **61** (2026) 7288. https://doi.org/10.1007/s10853-026-12248-3.

[20] D. Bai, D. Zheng, S. Yang, F. Yu, X. Zhu, L. Peng, L. Wang, J. Liu, D. Yang & S. Liu, "Surface modulation for highly efficient and stable perovskite solar cells", RSC advances **13** (2023) 28097. https://doi.org/10.1039/D3RA00809F.

[21] T. Kirchartz, "Challenges and opportunities for the characterization of electronic properties in halide perovskite solar cells", Chemical science **16** (2025) 8153. https://doi.org/10.1039/D5SC00504C.

[22] I. Levine, A. Al-Ashouri, A. Musiienko, H. Hempel, A. Magomedov, A. Drevilkauskaite, V. Getautis, D. Menzel, K. Hinrichs, T. Unold, S. Albrecht & T. Dittrich, "Charge transfer rates and electron trapping at buried interfaces of perovskite solar cells", Joule **5** (2021) 2915. https://doi.org/10.1016/j.joule.2021.07.016.

[23] E. Danladi, P. R. Jubu, A. M. Tighezza, I. Hossain, N. N. Tasie, M. O. Abdulmalik, A. C. Egbugha, M. O. Awoji, M. Kashif, E. D. Onoja, M. I. Amanyi & E. E. Oguzie, "Highly efficient, hole transport layer (HTL)-free perovskite solar cell based on lithium-doped electron transport layer by device simulation", Emergent materials **6** (2025) 1779. https://doi.org/10.1007/s42247-023-00558-0.

[24] E. Danladi, L. F. Obagboye, S. Aisida, F. I. Ezema, O. Okorie, J. A. Bwamba, P. A. Emmanuel, A. A. Hussaini, P. R. Jubu & A. C. Ozurumba, "20.730% highly efficient lead-free $CsSnI_3$-based perovskite solar cells with various charge transport materials: a SCAPS-1D study", Multiscale and multidisciplinary modeling, experiments and design **8** (2025) 114. https://doi.org/10.1007/s41939-024-00701-2.

[25] M. Stolterfoht, P. Caprioglio, C. M. Wolff, J. A. Márquez, J. Nordmann, S. Zhang, D. Rothhardt, U. Hörmann, Y. Amir, A. Redinger, L. Kegelmann, F. Zu, S. Albrecht, N. Koch, T. Kirchartz, M. Saliba, T. Unold & D. Neher, "The impact of energy alignment and interfacial recombination on the internal and external open-circuit voltage of perovskite solar cells", Energy & environmental science **12** (2019) 2778. https://doi.org/10.1039/C9EE02020A.

[26] A. Haddout, M. Fahoume, A. Qachaou, A. Raidou & M. Lharch, "Understanding effects of defects in bulk Cu_2ZnSnS_4 absorber layer of kesterite solar cells", Solar energy **211** (2020) 301. https://doi.org/10.1016/j.solener.2020.09.067.

[27] T. Minami, Y. Nishi & T. Miyata, "Efficiency enhancement using a $Zn_{1-x}Ge_x$-O thin film as an n-type window layer in Cu_2O-based heterojunction solar cells", Applied physics express **9** (2016) 052301. https://doi.org/10.7567/APEX.9.052301.

[28] P. Singh & N. M. Ravindra, "Temperature dependence of solar cell performance: an analysis", Solar energy materials and solar cells **101** (2012) 36. https://doi.org/10.1016/j.solmat.2012.02.019.

[29] M. T. Lloyd, J. E. Anthony & G. G. Malliaras, "Photovoltaics from soluble small molecules", Materials today **10** (2007) 34. https://doi.org/10.1016/S1369-7021(07)70277-8.

[30] S. S. Shin, B. W. Park, J. H. Noh & S. I. Seok, "Interlayer engineering in metal halide perovskite photovoltaics", Nature photonics **20** (2026) 11. https://doi.org/10.1038/s41566-025-01809-8.

[31] M. K. Hossain, M. S. Uddin, G. F. I. Toki, M. K. A. Mohammed, R. Pandey, J. Madan, M. F. Rahman, M. R. Islam, S. Bhattarai, H. Bencherif, D. P. Samajdar, M. Amammi & D. K. Dwivedi, "Achieving above 24% efficiency with non-toxic $CsSnI_3$ perovskite solar cells by harnessing the potential of the absorber and charge transport layers", RSC advances **13** (2023) 23514. https://doi.org/10.1039/D3RA02910G.

[32] S. Ahmed, F. Jannat, M. A. K. Khan & M. A. Alim, "Numerical development of eco-friendly Cs_2TiBr_6-based perovskite solar cell with all-inorganic charge transport materials via SCAPS-1D", Optik **225** (2021) 165765. https://doi.org/10.1016/j.ijleo.2020.165765.

[33] S. M. Liga & G. Konstantatos, "Colloidal synthesis of lead-free $Cs_2TiBr_{6-x}I_x$ perovskite nanocrystals", Journal of materials chemistry C **9** (2021) 11098. https://doi.org/10.1039/D1TC01732B.

[34] C. Kupfer, J. Elia, M. Kato, A. Osvet & C. J. Brabec, "Mechanochemical synthesis of cesium titanium halide perovskites $Cs_2TiBr_{6-x}I_x$ (x = 0, 2, 4, 6)", Crystal research and technology **58** (2023) 2200150. https://doi.org/10.1002/crat.202200150.

[35] W. Shockley & H. J. Queisser, "Detailed balance limit of efficiency of p-n junction solar cells", Journal of applied physics **32** (1961) 510. https://doi.org/10.1063/1.1736034.

[36] J. Wang, Z. Zheng, P. Bi, Z. Chen, Y. Wang, X. Liu, S. Zhang, X. Hao, M. Zhang & Y. Li, "Tandem organic solar cells with 20.6% efficiency enabled by reduced voltage losses", National science review **10** (2023) nwad085. https://doi.org/10.1093/nsr/nwad085.

[37] M. Saadat & S. Bameri, "Comprehensive analysis of transport layers and interface defects in $MAPbI_3$-based PSCs for enhanced efficiency", Discover applied sciences **7** (2025) 440. https://doi.org/10.1007/s42452-025-06948-9.

[38] S. Rühle, "Tabulated values of the Shockley–Queisser limit for single junction solar cells", Solar energy **130** (2016) 139. https://doi.org/10.1016/j.solener.2016.02.015.

[39] P. R. Jubu, S. K. Omotayo, E. E. Oguzie, T. Imbur & M. Z. Pakhuruddin, "High-efficiency HTL-free i-n versus p-i-n InGaN single junction solar cells: a SCAPS-1D optimization study", Next energy **11** (2026) 100540. https://doi.org/10.1016/j.nxener.2026.100540.

[40] H. Y. Najem, R. A. Rasool, M. N. Z. Mala & A. M. Saadi, "Temperature and spectral effects on perovskite solar cells: a SCAPS-1D simulation study", International journal of design & nature and ecodynamics **20** (2025) 1449. https://doi.org/10.18280/ijdne.200702.

[41] E. Danladi, W. Mutah, P. R. Jubu, K. A. Ogunmoye, Z. L. Abubakar, D. A. Bala, N. N. Tasiu, A. Idris, F. Aungwa, M. I. Amanyi, E. Akpogumah, N. I. Noah & F. Ezema, "Photovoltaic performance of $CsPbBr_3$-based perovskite solar cell with TiO_2 and quaternary chalcogenide Cu_2FeSnS_4 as charge transport channels: unlocking >26% efficiency via SCAPS-1D investigation", Next energy **9** (2025) 100423. https://doi.org/10.1016/j.nxener.2025.100423.

[42] P. K. Deendyal, S. Dhakla, R. Singla, A. Taya & M. K. Kashyap, "Perovskite solar cells without hole and electron transport layers", in *Perovskite solar cells: reshaping the future energy landscape*, M. Kumar & A. Raj (Eds.) Springer, Singapore, 2025, pp. 73 - 94. https://doi.org/10.1007/978-981-96-9463-1_4.

[43] M. A. Green, E. D. Dunlop, M. Yoshita, N. Kopidakis, K. Bothe, G. Siefer, X. Hao & J. Y. Jiang, "Solar cell efficiency tables (version 64)", Progress in photovoltaics: research and applications **32** (2024) 425. https://doi.org/10.1002/pip.3831.

[44] H. Son & B. S. Jeong, "Optimization of the power conversion efficiency of CsPbIxBr1-x-based perovskite photovoltaic solar cells using ZnO and NiOx as an inorganic charge transport layer", Applied sciences **12** (2022) 8987. https://doi.org/10.3390/app12188987.

[45] N. El Aallaoui, B. Oukarfi & M. Zazoui, "Numerical study of inorganic Cs_2TiBr_6 solar cells with double hole transport layers", Materials today: proceedings **66** (2022) 122. https://doi.org/10.1016/j.matpr.2022.04.010.

[46] A. O. Aransiola, K. I. Udofia, C. Amakom, P. R. Jubu, I. K. Nwokolo, J. O. Anyanwu, O. O. Ilori & E. E. Oguzie, "From record efficiency to commercially viable modules: a commercialization framework for stability-driven translation of perovskite solar cells", Next research **10** (2026) 1. https://doi.org/10.1016/j.nexres.2026.101856.